Effects of controlled vortex generation and interactions in transverse jets

Elijah W. Harris, Takeshi Shoji,* Andrea Besnard,† Stephen G. Schein, Robert T. M'Closkey, Luca Cortelezzi,‡ and Ann R. Karagozian§
Department of Mechanical and Aerospace Engineering, University of California, Los Angeles, Los Angeles, California 90095-1597, USA

(Received 4 August 2021; accepted 21 December 2021; published 18 January 2022)

This experimental study examined the effects of controlled vortex generation and interactions created by axisymmetric excitation of a transverse jet, with a focus on the structural and mixing characteristics of the flow. The excitation consisted of a double-pulse forcing waveform applied to the jet, where two distinct temporal square-wave pulses were prescribed during a single forcing period. The two distinct pulses produced vortex rings of different strength and celerity, the strategic selection of which promoted vortex ring interactions or collisions in the near field to varying degrees. Jet flow conditions corresponding to a transitionally convectively and absolutely unstable upstream shear layer (USL) in the absence of forcing, at a jet-to-cross-flow momentum flux ratio of $J = 10$, and to an absolutely unstable USL at $J = 7$, were explored for a jet Reynolds number of 1800. Acetone planar laser-induced fluorescence imaging was utilized to quantify the influence of different prescribed temporal waveforms. All forcing conditions enhanced the spread, penetration, and molecular mixing of the jet as compared to the unforced jet, though to differing degrees. Interestingly, when the jet was convectively unstable, forcing which promoted vortex collisions provided the greatest enhancement in molecular mixing, whereas the absolutely unstable jet produced the greatest enhancement in mixing when the vortex rings did not interact, with important implications for optimized jet control.

DOI: 10.1103/PhysRevFluids.7.013902

I. INTRODUCTION

The transverse jet, or jet injected normally into uniform cross-flow (JICF), is a canonical flow field within engineering research which has been studied extensively over the past 70+ years. The application base of the fundamental flow field is extremely wide reaching, spanning the realms of industrial, environmental, and biological systems, with a main facet of implementation being within air-breathing propulsion systems [1–4]. Even within an aircraft engine the applicability of the JICF varies greatly owing to the range of desired characteristics of the flow; in the combustion zone(s) of the engine it is desirable to have a jet which penetrates deeply and mixes rapidly with the cross-flow so as to promote more efficient combustion processes [5–7], whereas low penetration and a suppression of mixing is desirable for utilization in the turbine section for film blade cooling [8,9]. Moreover, implementation in the exhaust nozzle as a method of thrust vectoring or VSTOL would involve delicate tuning of the spread and penetration of the flow for specific

*Also at Japan Aerospace Exploration Agency, Tsukuba, Japan.
†Also at The Aerospace Corporation, Los Angeles, California, USA.
‡Also at Department of Aerospace Science and Technology, Polytechnic University of Milan, Milan, Italy.
§ark@ucla.edu

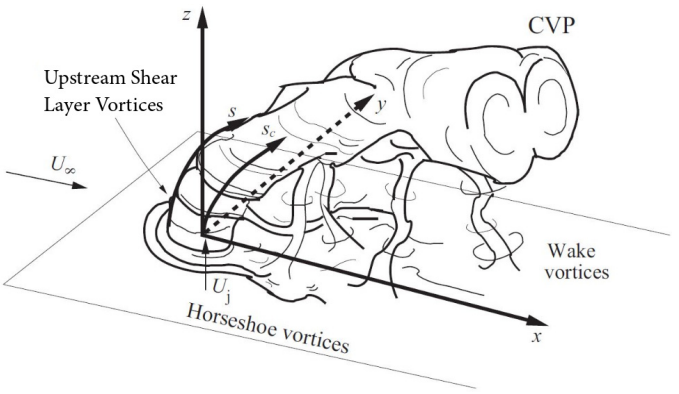

FIG. 1. Schematic of a flush round jet with mean velocity U_j injected normally into cross-flow of free-stream velocity U_∞, with representative depictions of the relevant vortical structures. Appropriate coordinate axes x, y, z, jet shear layer trajectory s, and jet center-line trajectory s_c are also shown. Adapted from [13].

control of the thrust [10–12]. In all cases, the flow field is represented by a highly complex and dynamically nonlinear three-dimensional flow system composed of a variety of vortical structures.

A representative depiction of the JICF is given in Fig. 1, where dominant vortex systems are shown, including the horseshoe vortex which wraps around the leading edge of the jet column and extends downstream, the shear layer vortices which form on the upstream side of the jet near the jet exit plane and convect along the shear layer, the upright wake vortices further downstream which entrain wall boundary layer fluid into the jet [13], and the counter-rotating vortex pair (CVP), which is the most dominant flow feature associated with jet cross section [14]. Characterization of the flow field is typically made with nondimensional parameters such as the jet-to-cross-flow velocity ratio ($R = U_j/U_\infty$), jet-to-cross-flow density ratio ($S = \rho_j/\rho_\infty$), jet-to-cross-flow momentum flux ratio ($J = \rho_j U_j^2/\rho_\infty U_\infty^2 = SR^2$), and jet Reynolds number ($\mathrm{Re}_j = \rho_j U_j D/\mu_j$), which is based on the jet exit diameter (D), bulk (spatially averaged) jet velocity (U_j), and jet absolute viscosity (μ_j).

Given the complexities and interdependencies associated with the system of vortical structures for the JICF, a number of recent studies have investigated the dynamics of the flow field experimentally [15–18], numerically [19–23], and theoretically [24–26]. In many of these studies there is special emphasis placed upon the upstream and downstream shear layer instabilities. For the equidensity ($S = 1$) JICF, Megerian *et al.* [15] show that these upstream shear layer (USL) instabilities undergo a transition from convective instability, where the instabilities are relatively weak with broadband spectral characteristics convected downstream, to absolute instability, where the instabilities are strong with pure-toned spectral characteristics which propagate throughout the entire flow field. This transition occurs as the momentum flux ratio is decreased to relatively low values ($J \lesssim 10$) for a fixed jet Reynolds number ($\mathrm{Re}_j = 2000$ for this study). Iyer and Mahesh [22] demonstrate via direct numerical simulations (DNS) very good qualitative and quantitative agreement with experiments in the transition of the shear layer instabilities for an equidensity JICF at $\mathrm{Re}_j = 2000$ with $R = 2$ ($J = 4$) and $R = 4$ ($J = 16$). These findings are important given that the shear layer instabilities govern the nature of shear layer rollup into vortex rings, where the general consensus has been that the azimuthal shear layer vorticity is tilted and folded as it convects downstream, subsequently serving as the main catalyst in the formation of the CVP [19,27,28]. In fact, Getsinger *et al.* [29] demonstrate a direct correlation between the strength of the shear layer instabilities and the development of the CVP structure, noting that there is a greater susceptibility to asymmetries when the shear layer is convectively unstable (CU), while an absolutely unstable (AU) shear layer produces a CVP which is quite symmetric. The strength and symmetry of the CVP is strongly correlated with the mixing characteristics between the jet and cross-flow, whereby as the CVP becomes more symmetric the molecular mixing of the flow field is enhanced [30].

With the aforementioned applications, and contrasting requirements for transverse jets in terms of spread, penetration, and mixing, many studies have sought to selectively optimize desired characteristics through active (temporal) control of the issuing jet, typically involving sinuous or simple square-wave excitation applied to the jet [15,31–38]. When axisymmetrically exciting the JICF with a sinusoidal waveform, it is seen that the flow can lock-in to the forcing, a phenomenon by which the upstream shear layer will synchronize to the forcing frequency f_f, overcoming and diminishing instabilities associated with the frequency of the natural instability mode f_o [36,39]. The exact behavior of this lock-in is dependent on the natural instability characteristics of the flow field, where an AU flow requires a higher amplitude of excitation at a given frequency to achieve lock-in than does a CU flow, and excitation frequencies further away from the natural instability frequency require stronger forcing than frequencies close to the natural instability. While this kind of lock-in behavior is often seen in absolutely unstable flows such as low density and reactive free jets [40] and wakes [41], it is unusual to observe this behavior when the flow is naturally convectively unstable. In addition to such unconditional lock-in, the transverse jet in some cases also displays marginal lock-in or quasiperiodicity at lower amplitude excitation, with instabilities identified at frequencies corresponding to linear combinations of f_f and f_o, as well as states in which the flow is completely nonresponsive to the excitation [39]. Recent work by Shoji *et al.* [37] demonstrates that low-level sinusoidal excitation can cause a transverse jet with a CU upstream shear layer to create a more symmetric jet cross section and enhance molecular mixing. They additionally note that once the jet's USL flow is AU (typically for $J \lesssim 10$), higher amplitude forcing is required to overcome the natural instability and synchronize or lock-in the flow to the forcing frequency, yet even with lock-in, relatively little improvement is seen in the molecular mixing, except for conditions creating a clearly symmetric CVP structure in the cross section, often for forcing frequencies close to the fundamental f_o. In contrast, application of temporal square-wave excitation to AU flows is found to produce distinct changes to the spread, penetration, and mixing at much lower forcing amplitudes than are required by its sinusoidal counterpart, where the root mean square (rms) of the velocity excitation is used to quantify amplitude. Square-wave excitation is effective for forcing frequencies both above and below the natural instability frequency [32,36,38]. In these recent studies, excitation conditions creating enhanced jet penetration and spread did not correlate directly with improved molecular mixing; there was a stronger correlation of improved mixing with creation of a more symmetric jet cross section, in some cases with a counter-rotating vortex pair structure.

When characterizing the square-wave excitation applied to the jet, a parameter of considerable significance is the temporal pulse width τ of the generated waveform, which is determined from the waveform duty cycle α and forcing frequency f_f, where $\tau = \alpha/f_f$. This leads to an expression for the transverse jet's effective nondimensional stroke ratio L/D,

$$\frac{L}{D} = \frac{1}{D}\int_0^{\tau} (u_j)dt, \tag{1}$$

where u_j is the mean subtracted temporal jet velocity at the exit plane, and D is the jet nozzle exit diameter. The stroke ratio is used to express a nondimensional universal timescale or formation number associated with piston-generated formation of a vortex ring [42], and has been implemented by others to describe pulsations associated with a fully modulated JICF [31,43]. In other studies where the transverse jet flow is not fully modulated, the effective stroke ratio is instead derived from a peak-to-peak velocity rather than the total velocity [33,35,36,38]. This alteration effectively enables L/D to quantify the net vortex formation number imparted to the jet due to the excitation alone, rather than the total introduction of jet fluid in the flow field. From the effective stroke ratio, the flow structures generated and vorticity imparted to the jet flow may be related to vortex ring formation phenomena of a starting jet [33,36,38,43].

For the isolated vortex ring or starting jet, Gharib *et al.* [42] determine an optimal stroke ratio exists at $L/D \approx 4$ such that the vortex ring produced is fully filled. For the vortex ring in cross-flow, however, the DNS study by Sau and Mahesh [44] shows that the presence of a cross-flow can result in a reduction of the optimal stroke ratio for the formation of a fully filled vortex ring structure.

They introduce a parameter called the ring velocity ratio r_{ring}, defined as the bulk peak-to-peak jet velocity divided by the cross-flow velocity

$$r_{\text{ring}} = \frac{\Delta U_j}{U_\infty}. \tag{2}$$

Sau and Mahesh [44] note that as the ring velocity ratio is decreased, the optimal stroke ratio decreases to a minimum value of $L/D \approx 1.5$, after which further reducing r_{ring} results in the production of hairpin vortices rather than coherent vortex rings. In the limit as the cross-flow velocity approaches zero, with an infinite r_{ring}, the optimal L/D approaches the "formation number," approximately 3.6. They also reason that for an isolated vortical structure in cross-flow, stroke ratios L/D greater than the optimal values for vortex ring formation, which produce a trailing column of jet fluid behind the fully filled vortex ring, should enhance the mixing process more than the fully filled and deeply penetrating ring, owing to an enhanced downstream entrainment of cross-flow from the trailing column.

Recent experiments by Shoji *et al.* [38] pertaining to square-wave excitation of a transverse jet for a range of momentum flux ratios and excitation conditions enables exploration of some of these ideas. For a JICF with a weak CU USL, the stroke ratio producing the best molecular mixing is very near the established value of $L/D \approx 4$ suggested by Gharib *et al.* [42] for a starting jet or isolated vortex ring. They also note that as the cross-flow is strengthened and the jet eventually transitions to an AU USL, the stroke ratio for optimum molecular mixing is reduced, and in addition that stroke ratios corresponding to the best jet spread and penetration, long thought of as indicators of improved jet, do not necessarily correspond to stroke ratios for optimal molecular mixing. For the fully modulated JICF, Johari [43] notes that differences in the jet penetration are attributable to the relative interactions between successive vortex structures, in which fully filled vortex rings, having a larger celerity than partially filled rings, interact sooner in the jet near field than partially filled vortex rings. Johari further postulates that selective determination of the pulsing parameters can achieve both initially deeply penetrating vortical structures in the near field, followed by interactions between these vortical structures for improved mixing by a prescribed downstream location. While the transverse jet experiments of Shoji *et al.* [38] explored square-wave excitation for a range of stroke ratios L/D and momentum flux ratios J, including naturally AU and CU upstream shear layers, no experimental study to our knowledge has explored controlled interactions between successive vortical structures, for either vortex rings or vortex rings with trailing columns.

This study is designed to explore the influence of controlled vortex generation and interactions on transverse jet structures, penetration, and especially molecular mixing. Vortical structures of differing strengths and separation distances are created using double-pulse square-wave temporal excitation of the jet fluid, wherein during a single forcing period $T = 1/f_f$, two distinct and independently controlled square-wave pulses can be generated. Hence, the independent pulses of vorticity can generate vortex rings of differing strengths and celerity so as to induce a fast propagating vortex ring catching up to a slower ring, yielding vortex interactions or collisions to promote vortex merger or breakdown, and thereby potentially enhancing the overall mixing process. Acetone planar laser-induced fluorescence (PLIF) imaging was used to explore structural and molecular mixing characteristics, as done in the past for both forced and unforced transverse jets [30,37,38]. The flow conditions here corresponded to the equidensity transverse jet with a naturally transitionally CU/AU USL at $J = 10$, and a naturally AU USL for $J = 7$, at a fixed jet Reynolds number of 1800. These studies enabled a systematic exploration of the potential for controlled vortex formation and interactions to impact important transverse jet global behavior.

II. EXPERIMENTAL SETUP AND METHODS

A. Transverse jet tunnel

Figure 2 schematically depicts the low-speed wind tunnel utilized for this experimental study. The apparatus operated in a nonrecirculating manner, where room air was continuously provided by

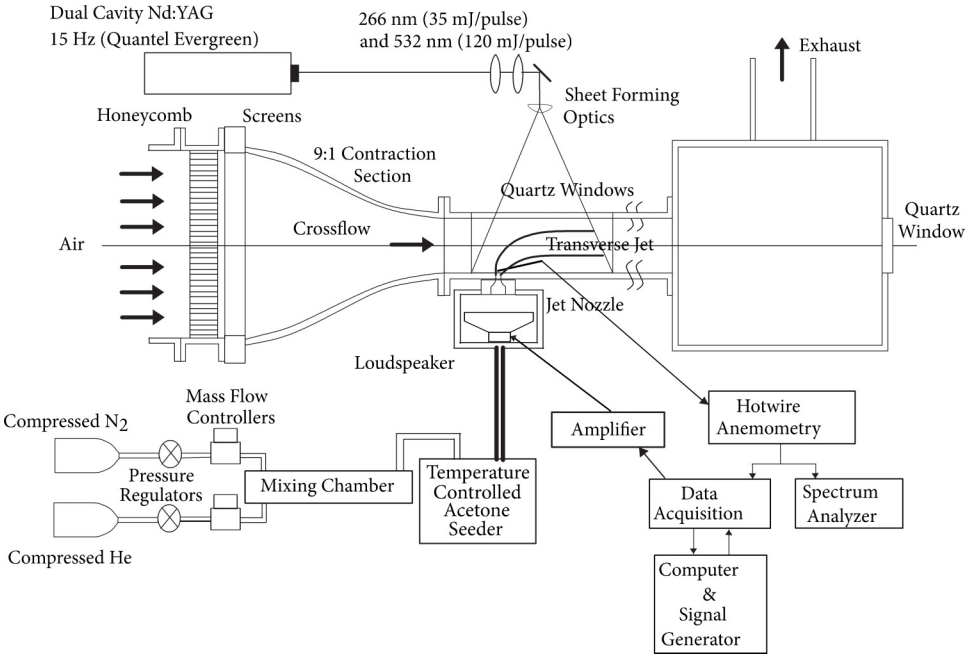

FIG. 2. Low-speed wind tunnel, laser system, hot-wire anemometry, and variable density jet injection comprising the experimental JICF configuration.

a centrifugal blower, and was later expelled to the building exhaust system via ducting at the end of the tunnel. The air drawn in from the blower was directed through a series of screens and honeycomb cells to condition the flow, after which it passed through a 9:1 area ratio contraction leading into the main test chamber. Such flow conditioning has been determined to result in a turbulence intensity level of less than 1.5% with a maximum free-stream tunnel velocity of $U_\infty = 7.00$ m/s, while measurements of the boundary layer within the main test section indicate a clear laminar Blasius profile for all cross-flow velocities considered [29]. Constituting the main test chamber was a black-anodized aluminum 12 cm × 12 cm × 82.5 cm rectangular tube. In combination with the black-anodized finish was a matte black heat-resistant coat of paint, both of which served to minimize laser sheet reflections and ablation due to light impingement at the tunnel surfaces. Access for the optical diagnostics was made possible through three cutouts along the sides of the tunnel. In the top, a fused silica quartz window was mounted to pass the UV laser light into the tunnel for illumination of the jet, while the sides were fitted with plexiglass panels providing optical access to the cameras. Additionally, when utilizing the hot-wire anemometer for characterization of USL spectral content and feed-forward convergence of the acoustic excitation waveforms, a panel with a small cutout was fitted in the side of the tunnel in place of the plexiglass to allow port access to the probe. To control any attenuation of the flow field within the main test section due to a pressure drop from the suction of exhaust system, a 30 cm × 30 cm × 63 cm wooden chamber was inserted between the tunnel and the exhaust ducting [45].

The jet fluid was comprised of nitrogen, helium, and acetone vapor, the latter of which served as the tracer particle for the PLIF imaging. The bulk fluid properties of the jet were determined based on the individual fluid properties and mole fractions for each of the respective species, the exact methodology of which is detailed in Gevorkyan [45]. Careful consideration was made for the acetone vapor to maintain its mole fraction below the critical threshold of a saturated vapor concentration at room temperature and pressure so as to prevent condensation in the jet. The flow rates for the N_2 and He were determined *a priori* based on the desired jet bulk fluid properties, and

were independently maintained by mass flow controllers (Tylan Model FC-260) and were mixed through a packed bed passive mixing chamber. Seeding of the acetone tracer was then achieved by passing the N_2 and He gas mixture through a temperature-controlled seeding chamber which was monitored by a T-type thermocouple and a pressure transducer (Omega PX409-015G5V). Flow from the seeding chamber was passed to small plenum just upstream of the injection plane wherein a 4-in. loudspeaker (RadioShack 40-1022B, 4-in. woofer) was housed, which provided the acoustic excitation of the jet flow. Downstream of the plenum, the jet was injected to the main test chamber through a 16:1 area contracting nozzle with a fifth-order polynomial interior profile and an exit diameter of 7.59 mm. The nozzle exit plane was mounted flush with the tunnel floor, and produced a top-hat velocity profile in the absence of a cross-flow [15,46]. In all cases, the resulting jet had a density ratio of $S = 1$, and a jet Reynolds number of $\mathrm{Re}_j = 1800$. Two different flow conditions were treated: a jet with a transitionally CU/AU USL at $J = 10$, and one with an AU USL at $J = 7$, each with an acetone mole fraction of $\psi = 0.218$, and a fixed bulk jet velocity of $U_j = 3.31$ m/s. Variations to the momentum flux ratio were accomplished by maintaining the jet flow conditions and varying the cross-flow velocity U_∞.

B. Hot-wire anemometry

A single-component boundary-layer-type hot-wire anemometry probe (Dantec 55P15) was utilized to evaluate the spectral characteristics along the USL of the jet. The probe was inserted from the side of the test chamber through a port access, and was oriented such that the wire was parallel with the free-stream cross-flow. Translation of the probe in the x, y, and z directions, with an accuracy of 1 μm (1.32×10^{-4} jet diameters), was possible via Newport high-performance low-profile ball-bearing linear stages constructed in a triple axis traversing platform system. The shear layer spectral characteristics were based on the vertical velocity fluctuations as the hot-wire was traversed downstream along the jet USL (s/D). The output signal from the probe was sent to a 90C10 constant temperature anemometry (CTA) module in a Dantec StreamLine 90N10 frame, after which the ac and dc components of the signal were separated and conditioned via a signal conditioning system created by Hendrickson [47]. Finally, the ac component of the conditioned signal was sent to a dynamic signal analyzer (HP-35665A), which takes in the raw hot-wire signal (acquired at 20 kHz) and then outputs the power spectrum of the time signal over a 6.4-kHz range with 8-Hz resolution. Details regarding the determination of the shear layer trajectory, calibration of the hot-wire probe, and other aspects of the hot-wire system may be found in Shoji [48].

C. Waveform generation and adaptive feed-forward control

Generation of the excitation waveform applied to the jet fluid was made by a loudspeaker (RadioShack 40-1022B, 4-in. woofer) housed in a plenum chamber just upstream of the jet nozzle, and was driven by an amplifier (Adcom GFA-7300) with a constant signal gain of 30. To produce the waveform, a data acquisition (DAQ) board (dSPACE 1104) was used with CONTROLDESK software within Matlab's SIMULINK to send the signal from the computer to the speaker. Measurements of the resultant oscillations in the flow at the jet exit were made by the hot-wire anemometry system, where the hot-wire was centered over the jet exit at 0.1 diameters above the exit plane. Digital sampling of the analog signal was made at 20 kHz with with the largest uncertainties in the velocity fluctuations on the order of 1% for a velocity of 1 m/s, as documented in prior studies [29].

The double-pulse forcing consisted of two independently controllable square-wave pulses generated during a single forcing period. The fundamental forcing frequency was $f_f = 55$ Hz, selected to match the square-wave forcing conditions explored in prior experimental excitation studies [32] for similar flow field parameters as those treated here (Re_j, J, S). Due to the complex nature of the waveform, the signal was created through a Fourier series of sinusoids at the fundamental forcing frequency and its 14 subsequent higher harmonics. Details regarding the determination of the number of harmonics and the selection of the harmonics to utilize in the Fourier series

composition of the waveform are the subject of an ongoing study, though it is noted that 15 sinusoidal inputs were determined to be sufficient to create reasonably accurate double-pulse square waves, as will be shown. Each of the 15 sinusoidal inputs was decomposed into respective $\sin(kf_f t)$ and $\cos(kf_f t)$ functions, with $f_f = 55$ Hz and $k = 1, 2, \ldots, 15$, so that respective adjustments in the amplitudes of these functions translated to alterations in the amplitude and phase of the original signal components. For all forcing cases considered, the rms of the perturbation, defined in Eq. (3) below,

$$u'_{j,\mathrm{rms}} = \sqrt{\frac{1}{T}\int_{t_1}^{t_1+T} (u_j - U_j)^2 dt}, \tag{3}$$

was matched for each individual pulsation so that the effective level of forcing applied, or the effective impulse imparted to the jet fluid for each pulsation, was the same for all waveforms. The perturbation rms applied to the jet was chosen as $u'_{j,\mathrm{rms}} = 2.0$ m/s, corresponding to a relative excitation of $u'_{j,\mathrm{rms}}/U_j = 0.60$. Additionally, the mean velocity of the excitation was set to 0 m/s so that the net flow of the forced jet was comparable to the unforced case. With both the perturbation rms and mean of the excitation fixed, the only other independent parameters needed to characterize the double-pulse forcing waveform were the temporal pulse widths for each pulse, τ_1 and τ_2, as well as the temporal spacing between the two pulses, $\Delta\tau$; the pulse amplitudes were defined as a function of the other parameters.

Complicating the waveform formation were the inherent nonlinearities of the experimental setup, the imperfect nonflat frequency response of the actuation system, and the nonlinear behavior of the JICF itself [32,33,36,38]. Earlier studies improve the jet's temporal waveform in response to these issues via a feed-forward controller based on a mathematical inversion of a linear representation of the frequency response of the actuation system [32,33]. Later experiments use a truncated Fourier series to define the waveform, where each of the inputs' amplitudes and phases are adjusted based on a linear best fit to the empirical frequency response of the actual jet waveform at the selected Fourier series frequencies of interest [36]. This method eliminates the feed-forward element present in the prior approach, and thus does not account for other disturbances that are present, but still generally approximates the idealized square wave. Most recently, Shoji *et al.* [38] extends this truncated Fourier series approach to an adaptive feed-forward control method and is able to converge to well-refined waveforms. This methodology was implemented in this study to generate the double-pulse forcing waveforms.

After the double-pulse waveform was mathematically prescribed, initial inputs for the 30 $\sin(kf_f t)$ and $\cos(kf_f t)$ functions, constituting the decomposed 15-term Fourier series, were established based on the desired jet velocity components and the estimated frequency response of the actuator system at the selected fundamental forcing frequency and higher harmonics. The estimation of the frequency response was determined from correlating the hot-wire-based jet velocity measurements with sinusoidal excitation of the jet at the frequencies of interest. Additionally, a low-pass filter (first-order Butterworth filter) at a corner frequency of 600 Hz, $\approx 11 f_f$, was applied to the desired waveform to reduce the effects of the higher-order harmonics on the production of high-frequency noise. With the initial inputs therefore defined, the actuator system was modeled as a continuously differentiable function, and the waveform inputs were individually perturbed while monitoring the jet velocity output such that a perturbation matrix, the Jacobian of the modeled actuator system, could be experimentally determined. The perturbation magnitudes of all 30 signal components were each set relative to the magnitude of the actual input so as to prevent overly large perturbations from being applied to the more sensitive harmonics. The updated waveforms were then compared with the desired waveform output to determine if it was sufficiently converged or if further iterations were necessary. Convergence was achieved when the output amplitudes of the 30 sine and cosine functions, as determined from a fast Fourier transform (FFT) of the actual waveform, deviated less than 10^{-3} from the prescribed amplitudes for the ideal waveform. This typically took fewer than 5 iterations.

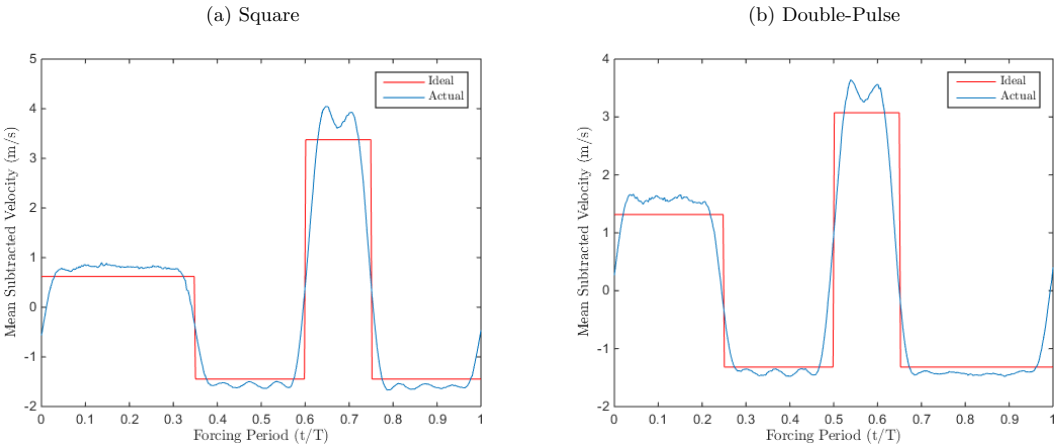

FIG. 3. Representative depictions of actual forcing waveforms compared with their respective ideal waveforms for double-pulse forcing waveforms corresponding to (a) case 2a, and (b) case 3a, both with a mean subtracted perturbation amplitude of $u'_{j,\mathrm{rms}} = 2.00$ m/s.

Figure 3 represents sample ideal square-wave and double-pulse forcing waveforms, along with their respective final converged waveforms as measured by the hot-wire anemometer just above the jet exit. The converged waveforms typically had very clean and sharp temporal upsweeps and downsweeps, though some slight ringing could be noted in the peaks. This small ringing was not easily eliminated given the complexity of the waveforms and the waveform being generated by a truncated Fourier series of only 15 terms. Prior studies, however, have deemed the waveform imperfections to be of little effect on jet response to forcing given that the predominant significance lies with the coherence of the upsweep and downsweep, and the resulting net stroke ratio, ring velocity ratio, and imparted circulation to the generated vortex ring [35,38].

Table I lists the set of double-pulse forcing waveforms implemented in this study, defining the temporal pulse widths of each pulse, and the temporal spacing between the two pulses [49]. The

TABLE I. Input test matrix of the various double-pulse forcing waveforms generated from a Fourier series of $f_f = 55$ Hz + 14 higher harmonics, while matching the rms of the jet velocity perturbation both temporal pulses at $u'_{j,\mathrm{rms}} = 2.0$ m/s. The temporal pulse widths of the first and second square-wave pulses are defined by their duration normalized over a single forcing period, as is the temporal spacing between the two pulses.

Case	Forcing	$\tau_{\mathrm{input},1}/T$	$\tau_{\mathrm{input},2}/T$	$\Delta\tau_{1\to2}/T$	$\Delta\tau_{2\to1}/T$
1a	0.45.70.85	0.45	0.15	0.25	0.15
1b	0.45.60.75	0.45	0.15	0.15	0.25
1c	0.45.55.70	0.45	0.15	0.10	0.30
2a	0.35.60.75	0.35	0.15	0.25	0.25
2b	0.35.50.65	0.35	0.15	0.15	0.35
2c	0.35.45.60	0.35	0.15	0.10	0.40
3a	0.25.50.65	0.25	0.15	0.25	0.35
3b	0.25.40.55	0.25	0.15	0.15	0.45
3c	0.25.35.50	0.25	0.15	0.10	0.50
4a	0.15.40.55	0.15	0.15	0.25	0.45
4b	0.15.30.45	0.15	0.15	0.15	0.55
4c	0.15.25.40	0.15	0.15	0.10	0.60

naming convention derived for the double-pulse forcing was based on the initiation and termination of the two square-wave pulses during a single forcing period. For example, case 1a (0.45.70.85) notes the first pulse initiates at $t/T = 0.0$ and terminates at $t/T = 0.45$, having a duration of $\tau_{\text{input},1}/T = 0.45$, and then the second pulse initiates and terminates at $t/T = 0.70$ and $t/T = 0.85$, respectively, representing a pulse duration of $\tau_{\text{input},2}/T = 0.15$ with a temporal delay after the first pulse of $\Delta\tau_{1\to2}/T = 0.25$. Given the desire for the double-pulse forcing to explore a fast-moving vortex catching up to and interacting with a slower-moving vortex that was generated earlier, the naming convention was also ordered such that the slower pulse, characterized by the longer of the pulse durations, was first and the faster (shorter) pulse was second. As indicated in the table for the results shown here, the second pulse duration was attempted to be fixed, while the first pulse duration, as well as the pulse separations, were varied. Per the matching of $u'_{j,\text{rms}}$, when a pulse's duration was shortened, the amplitude increased, and vice versa, enabling control of the creation and interaction of vortices at the jet exit.

D. Optical diagnostics

Acetone planar laser-induced fluorescence (PLIF) imaging served as the main diagnostic tool of this study, where jet structural characteristics and mixing quantification could be extracted from the scalar images. The main light source, depicted in Fig. 2, was a dual-cavity Q-switched Nd:YAG laser (Quantel Evergreen). Each cavity produced light in the IR at 1064 nm, which was then passed through harmonic generators to produce light in the green at 532 nm and the UV at 266 nm, with the latter serving to excite the acetone tracer in the jet. Green laser light is utilized in separate experiments involving particle image velocimetry (PIV) [46,50]. Triggering of the laser cavities was possible up to a maximum of 15 Hz, however, the internal optics of the laser were optimized for the best UV energy output, and optimal UV to green signal-to-noise ratio (SNR), when operating at 5 Hz. At this operating condition, each of the laser cavities was individually capable of producing 8 ns full width at half-maximum pulses with UV energy levels of approximately 30–35 mJ. The collimated laser beam was passed through a pair of dichroic mirrors in order to separate out the green light from the UV, and further improve the UV to green SNR. The beam was then passed to a focusing optic and a turning mirror which redirected the beam into the test section through a fused silica quartz window in the top of the tunnel. Just prior to entering the tunnel, the beam was spread into a sheet via an $f = -10$ mm UV optimized cylindrical lens, which was able to be rotated to create a sheet in the jet center-plane or cross section. The focal point was maintained near the tunnel floor so that a thin sheet was achieved throughout the entire imaging field of view (FOV). Investigation of the sheet thickness via the knife-edge technique determined a sheet thickness of $\approx$1 mm for the FOV of interest in this study.

Precise triggering was maintained through synchronization of the laser with the camera system, both of which were controlled by a programmable external timing unit (PTU) and LaVision's DAVIS 8.2 software. The triggering was not a rational multiple of the fundamental forcing frequency so as to not result in phase-locked imaging of the forced jet, however, there was slight leeway in this selection because of an inherent temporal shift in the optical setup (laser, camera, and PTU) between shots. A repetition rate of 1 Hz was selected such that an effective phase scanning or phase progressing imaging was achieved when the jet flow was locked in or synchronized to the forcing frequency, where successively recorded images were separated by a phase difference of 3.6°, which resulted in approximately 100 images recorded over a single temporal period. The recorded data sets consisted of 600 instantaneous snapshots which was well above the number required to achieve statistical convergence of the image data [48].

The imaging was performed with a 14-bit charge-coupled device (CCD) camera (LaVision Imager proX) with image resolution of 1600×1200 pixels, which was mounted to an external image intensifier (LaVision IRO) to further improve the SNR. The lens mounts for center-plane and cross-sectional imaging of the jet were different as a result of the different focal lengths

from the camera to the imaging plane and differences in the desired FOV. For center-plane imaging a Nikon 500 lens at f/2.0 with a Vivitar +2 dioptre closeup lens was used, while in the cross section a Nikon 200-mm lens at f/4.0 was implemented. Both configurations utilized a band-pass filter to help isolate the fluorescence signal. The raw images were postprocessed through a number of procedures including 2×2 binning, noise-bias correction, flat-field correction, background subtraction, laser energy absorption correction, and a dual-pass filtering. In the case of the laser energy absorption correction, a portion of the laser beam (approximately 7%) was split off and sent to a pyroelectric joulmeter (Newport 818E-10-50-S) for shot-to-shot energy measurements to adjust for fluctuations in the laser energy. After processing, the final resolution of the images yielded pixel sizes of 60–100 μm for both center-plane and cross-sectional FOVs. Details regarding these processes, and representative effects on the images, are documented in Shoji [48].

E. Mixing metrics

Historical metrics utilized to quantify the degree of mixing between the jet and cross-flow include the jet spread, penetration, and center-line concentration decay [1,36,51]. These methods are based on the mean characteristics of the jet, though it is well known [52] that instantaneous features are important for a complete understanding of molecular mixing associated with transitional or turbulent flow fields. In addition, such mean metrics are based on the center-plane view of the jet, which provides a limited perspective of the evolving jet, given that the majority of the jet fluid is located in the spanwise dimension outside of the JICF center-plane. Cross-sectional transverse jet imaging has enabled some researchers to utilize the spatial probability density function of the concentration to quantify molecular mixing trends [51,52]. More recent experiments by Gevorkyan *et al.* [30] systematically examine several alternative mean and instantaneous mixing metrics in both center-plane and cross-sectional dimensions, and find that molecular mixing can accurately be quantified via the unmixedness parameter U, which examines statistics associated with the second moment or variance of the scalar field at a given location. This parameter has been used quite successfully in a number of recent studies on the JICF [37,38,50,53].

The local unmixedness U_{xz}, evaluated at a location x in the x-z plane, can be represented by Eq. (4), for example, from an instantaneous center-plane PLIF image:

$$U_{xz} = \frac{1}{L_x L_z} \iint \frac{\left(\frac{C}{C_o} - \frac{\overline{C}}{C_o}\right)^2}{\frac{\overline{C}}{C_o}\left(1 - \frac{\overline{C}}{C_o}\right)} dx\, dz. \tag{4}$$

Here, C represents a local pixel element concentration at location (x, z) (i.e., the pixel value associated with acetone fluorescence imaging), $\overline{C}$ represents the spatially averaged concentration over the interrogation area $L_x L_z$, and C_o is the concentration value at the jet exit, in the potential core region, which is applied as a scaling factor. $L_x L_z$ represents the physical size of the interrogation area over which the analysis is being performed, in this case, a thin ($L_x = 7$ pixel-wide) slice of the jet in its center-plane, where L_z is the vertical domain of the field of view captured in the images. As done in earlier studies [30,48], L_z is adjusted by adding or subtracting zero-valued pixels to enable the mean concentration $\bar{C}$ to be equivalent for all x locations and for all conditions explored in the study, in order to compare mixing statistics appropriately. With this mixing metric, lower unmixedness values correspond to improved relative molecular mixing [54]. Cross-sectional unmixedness was also evaluated in the y-z plane for multiple downstream locations x. Unmixedness evaluations for both U_{xz} and U_{yz} were then applied to each instantaneous image and averaged over the number of realizations at a given location, producing an evaluation of local averaged unmixedness. Additional details regarding the unmixedness parameter and procedures for its implementation, along with details on other mean and instantaneous mixing metrics applied to the JICF, are given in Gevorkyan [45] and Shoji [48].

III. RESULTS

A. Spectral measurements

The stability characteristics of the transverse jet along its USL have been extensively studied for a variety of Re_j, J, S, and jet injector geometry configurations [15–18,29,39,50]. As noted previously, USL instabilities are known to undergo a transition from convective instability at larger momentum flux ratios to absolute or global instability as J is reduced via increases in cross-flow velocity. For the acetone-seeded equidensity ($S = 1$) flush nozzle-injected jet at a small diameter ($D = 4.04$ mm) with fixed $\mathrm{Re}_j = 1900$, the transition takes place at a critical momentum flux ratio of $J_{cr} \approx 9$ [18], while for the same mean flow conditions and nozzle injector, but without the presence of the acetone vapor, the transition occurs near $J_{cr} \approx 10$ [15,16]. Shoji *et al.* [18] find that this small change in the critical condition for USL transition arises from changes in the bulk viscosity of the jet fluid with the introduction of acetone, causing small alterations in the USL velocity profile and hence momentum thickness when jet Reynolds number is fixed. There is also a change in the dominant instability frequency of the USL with changes in the constituent species. Separate linear stability analysis (LSA) by Souza *et al.* [26] demonstrates that the instability characteristics of the JICF, and the critical transition from a CU USL to an AU USL, are dependent on the momentum thickness of the issuing jet, and hence viscous effects and finite Reynolds number, in addition to jet curvature effects. Because the USL instability characteristics for a larger flush nozzle ($D = 7.59$ mm) utilized in this study have not been investigated beyond the preliminary studies in early jet control experiments [32,33], we seek a more detailed exploration of such characteristics.

Figure 4 depicts contour plots of the shear layer spectra based on the hot-wire-based vertical velocity fluctuations measured along the USL trajectory of the present flush nozzle-injected JICF, with the strength of the instabilities indicated by the color bar for a given USL location s/D and scaled frequency, given in terms of the Strouhal number $\mathrm{St} = fU_j/D$. A fixed $\mathrm{Re}_j = 1800$ and acetone mole fraction of $\psi = 0.218$, for a range of momentum flux ratios, was explored by varying the cross-flow velocity. At $J = 15$ and 10, shown in Figs. 4(a) and 4(b), respectively, the spectral content was represented by relatively broadband instability peaks initiating around $s/D \approx 0.7$–1.0. Further downstream near $s/D \approx 1.5$, a dominant subharmonic peak emerged, with relatively weak or nonexistent higher harmonics regardless of s/D location. These characteristics are well-established identifiers of a CU USL [15–17]. Interestingly, the CU USL flows in Figs. 4(a) and 4(b) did not exhibit the same degree of frequency shifting in the instabilities observed in earlier transverse jet studies for a smaller flush nozzle to result from a tonal interference between the hot-wire and the jet, despite similar nondimensional flow conditions to the present experiments [18]. This weakening of the tonal interference was consistent with the doubling of the jet diameter (from 4.04 to 7.59 mm), while the length of the hot-wire probe remained constant at 1.25 mm; reducing the probe's relative size is known to result in the weakening of the tonal interference between the probe and the shear layer [55]. As cross-flow velocity was increased and momentum flux ratio reduced, e.g., as in Fig. 4(c) for $J = 7$, the dominant instability initiated closer to the jet exit (at $s/D \approx 0.5$), and was stronger and more pure toned than in Figs. 4(a) and 4(b). There was also an emergence of peaks at higher harmonics and correspondingly an elimination of the subharmonic peak. These traits in the shear layer spectra were indications that the JICF USL was being transitioned from convective instability to absolute or global instability [15,18,29]. As the momentum flux ratio was further reduced to $J = 3$, shown in Fig. 4(d), the instability characteristics depicted even stronger qualitative instability features, consistent with an AU flow. Hence, based on typical USL criteria, $J = 15$ and 10 were deemed to be CU.

Figure 4 also demonstrated a systematic increase in the Strouhal number of the fundamental instability, from $\mathrm{St} = 0.94$ to 1.24, as J was decreased from $J = 15$ to 7, where the jet transitioned from convective to absolute instabilities in the USL. Beyond this transition, further decreasing J decreased the dominant Strouhal number from the peak value at $J = 7$, to $\mathrm{St} = 0.78$ at $J = 3$. Megerian *et al.* [15] and Shoji *et al.* [18] note a similar peaking of the dominant instability frequency at the transition point between a CU and AU JICF for a range of jet flow conditions, with and

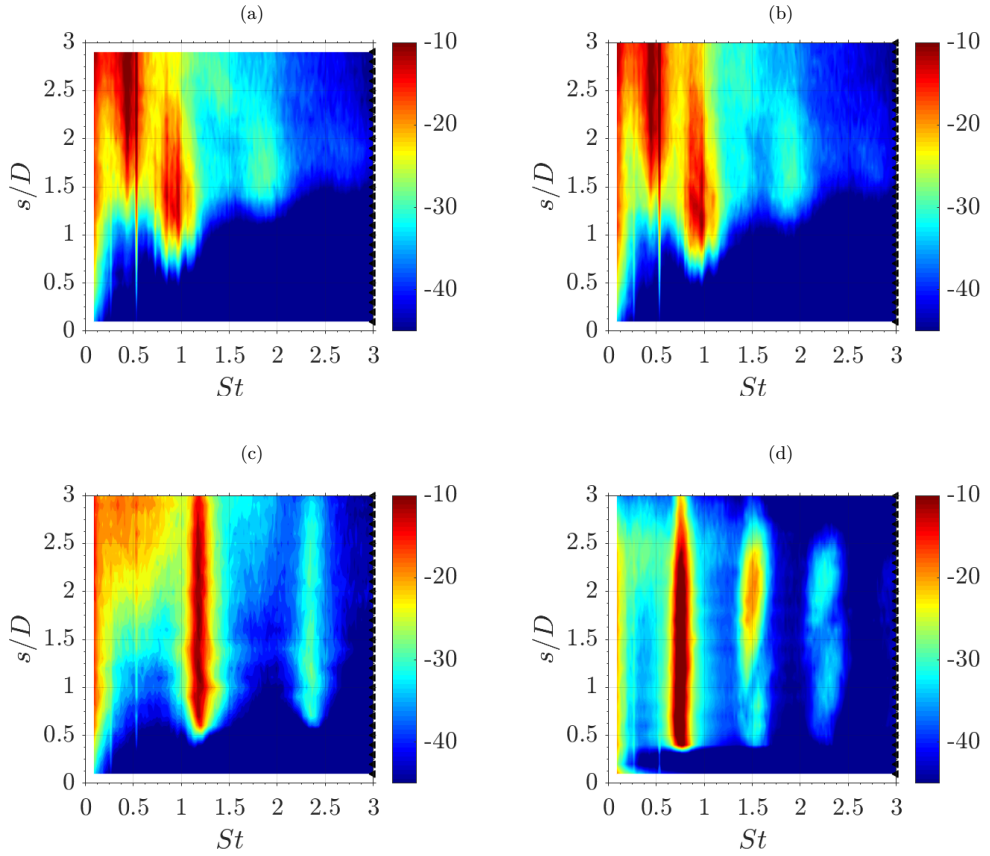

FIG. 4. Power spectra of the upstream shear layer instabilities for the equidensity large ($D = 7.59$ mm) flush nozzle-injected JICF with acetone mole fraction of $\psi = 0.218$, jet Reynolds number of $\mathrm{Re}_j = 1800$, and jet velocity of $U_j = 3.31$ m/s at momentum flux ratios of (a) $J = 15$ with a fundamental frequency of $f_0 \approx 410$ Hz, (b) $J = 10$ with $f_0 \approx 420$ Hz, (c) $J = 7$ with $f_0 \approx 540$ Hz, and (d) $J = 3$ with $f_0 \approx 340$ Hz.

without acetone tracer. Both experiments by Shoji *et al.* [18] and the LSA of Souza *et al.* [26] indicate that the variability in frequencies associated with these dominant instabilities for lower J values may be traced to competing dynamics of an increase in the jet momentum thickness and a strengthening of a countercurrent shear layer (CCSL-like) behavior at the USL as cross-flow velocity U_∞ increases. The CCSL behavior originates from the small negative velocity component induced by the recirculation zone upstream of the leading edge of the jet as the cross-flow velocity increases (decreasing J), explored in detail in Shoji *et al.* [18]. The findings on changes in the dominant or fundamental instability frequency were thus consistent with prior trends, in addition to being important in planning the present forced excitation experiments. Shoji *et al.* [39] note that for sinusoidal excitation, forcing frequencies f_f that are further away from the fundamental natural instability f_0 have greater difficulty in producing lock-in of the shear layer instability to the excitation frequency. The same is true for frequencies which are below the fundamental; both of these features contribute to distinctly asymmetric "V-shaped" lock-in diagrams for the JICF. Given the double-pulse forcing cases had a base forcing frequency of $f_f = 55$ Hz, transverse jet flow conditions with $J = 10$ and 7 were selected to be explored, since they not only straddled the boundary between convectively and absolutely unstable USL conditions, but also had dominant fundamental instability frequencies which were relatively close to one another. Further, the forcing amplitude in present studies was maintained at $u'_{j,\mathrm{rms}} = 2.0$ m/s, representing an excitation of just

TABLE II. Experimentally measured double-pulse forcing temporal pulse widths, stroke ratios, and ring velocity ratios for $J = 7$ with $U_j = 3.31$ m/s, $U_\infty = 1.22$ m/s, and excitation at $u'_{j,\mathrm{rms}} = 2.0$ m/s.

Case	$\tau_{\mathrm{actual},1}/T$	$\tau_{\mathrm{actual},2}/T$	L_1/D	L_2/D	$r_{\mathrm{ring},1}$	$r_{\mathrm{ring},2}$
1a	0.50	0.19	4.07	2.86	2.78	5.11
1b	0.50	0.19	4.09	2.85	2.80	5.11
1c	0.49	0.19	4.03	2.87	2.83	5.13
2a	0.39	0.19	3.69	2.79	3.18	4.96
2b	0.40	0.19	3.73	2.79	3.17	4.97
2c	0.39	0.19	3.67	2.81	3.20	4.98
3a	0.30	0.19	3.24	2.70	3.72	4.76
3b	0.30	0.20	3.22	2.69	3.70	4.72
3c	0.29	0.19	3.18	2.69	3.75	4.79
4a	0.20	0.20	2.60	2.56	4.50	4.48
4b	0.20	0.20	2.59	2.55	4.47	4.46
4c	0.20	0.19	2.56	2.54	4.50	4.50
Uncertainties	±0.0010	±0.0001	±0.08	±0.04	±0.03	±0.08

over 60% of the unforced jet velocity, well above the thresholds for lock-in documented for the JICF in Shoji *et al.* [39]. An exploration of the jet's lock-in characteristics and its dependence on the waveform generation methodology for double-pulse forcing are the subject of a separate investigation.

B. Structural characteristics

To visualize the structural characteristics of the unforced and double-pulse forced JICF, acetone PLIF images were recorded in the center-plane of the jet and at discrete vertical slices of the jet cross section at several different downstream locations. Due to the phase progressing representation of the acoustically excited jet data sets, where successive images were separated by a phase difference of $\theta \approx 3.6^\circ$ but were acquired just over 11 forcing periods apart, the pseudo-time-resolved data were able to illustrate the near-field evolution and interaction of vortical structures. Such imaging of vortical structures was not possible further downstream, where there was more turbulence and the flow behavior was more chaotic. In the case of the unforced jet, the natural instability frequency was not distinct nor strong enough to enable phase locking or phase progressing imaging of the jet, and as such the recorded images were simply representative snapshots at random phases over the natural jet evolution. For the cross-sectional slices, only images taken at $x/D = 0.0$ and 0.5 are shown, given the distinct focus on the generation, evolution, and eventual interaction of vortical structures in the jet near field.

As noted above, the forcing cases dealt with a "quick-pulse" fixed prescribed (input) temporal pulse width of $\tau_2/T = 0.15$, while the scaled temporal pulse width of the "slow pulse" (τ_1/T) and the temporal spacing between the two pulses ($\Delta\tau_{1\to2}/T$) were both varied. Table II lists the actual temporal pulse widths (τ_{actual}) as measured by the hot-wire anemometer placed just above the nozzle exit at $z/D = 0.1$, for experiments involving $J = 7$ excitation, for example. The pulse widths were slightly larger than their prescribed values given in Table I by about $\Delta\tau/T = 0.05$ due to the imperfect nature of the jet responsiveness to the impulsive upsweeps and downsweeps of the forced waveform and, as such, the temporal spacing between the pulsations was decreased. Shoji [48] demonstrates that these artifacts can be mitigated through adjustments to the way in which the waveform is generated, though this is often at the expense of overshoot and/or ringing in the waveform or greater complexity in building the waveform. The stroke ratios in Table II were determined from integration of the temporal jet velocity over the duration of the temporal pulse width,

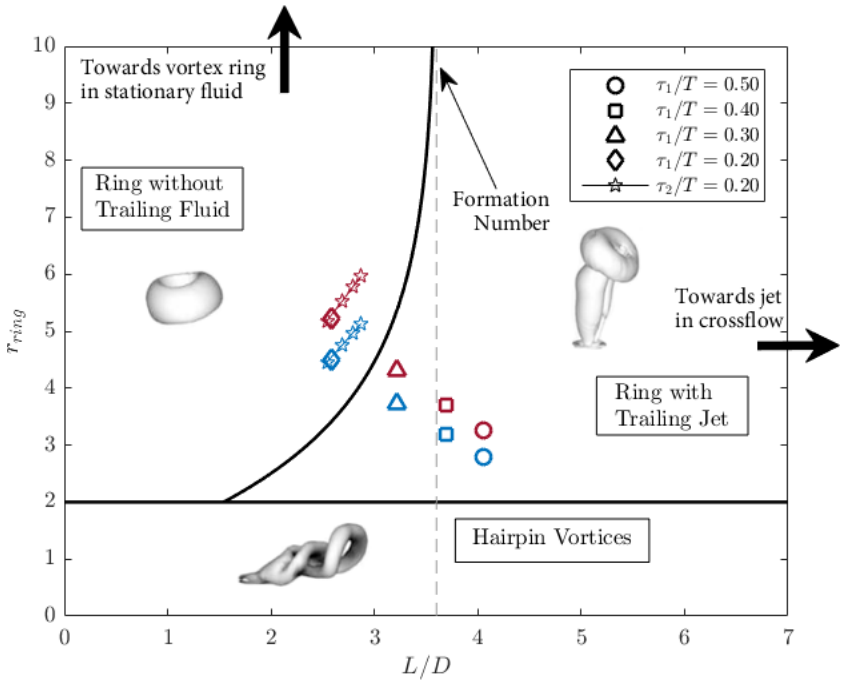

FIG. 5. Regime map of types of vortex rings formed based on the stroke ratio and ring velocity, with boundaries based on DNS of isolated vortex rings in cross-flow ([44]). The L/D and r_{ring} values for different temporal pulse widths in the present experiments are shown for cases with $J = 7$ (blue) and $J = 10$ (red).

as defined in Eq. (1), and the ring velocity ratios were established from Eq. (2). This formulation of the stroke ratio is utilized by others for flows which are also not fully modulated [36,47], and was selected for our specific interest in the formation of the vortical structures as they related to the different regimes of vortex ring formation for a transverse jet [35,44]. The uncertainties given in Table II for the pulse widths, stroke ratios, and ring velocity ratios represented the maximum bounds required across all forcing cases to establish 95% confidence intervals, based on evaluation of 15-s time-series acquisitions of the forced jet, hence with 825 forcing periods for each excitation case.

Figure 5 illustrates the different vortex ring regimes established by Sau and Mahesh [44] from their DNS-based results for the vortex ring injected into cross-flow, for a range of ring velocity ratios r_{ring}, and effective stroke ratios L/D. The regime below $r_{\text{ring}} = 2.0$ is characterized by connected hairpin vortices, while the upper left and right regimes delineate vortex rings without and with jet trailing columns, respectively. The dashed line represents the formation number as $r_{\text{ring}} \to \infty$, asymptotically approaching a starting jet behavior. Values of ring velocity and stroke ratio associated with the vortices generated in the present experiments, labeled according to their scaled pulse width (e.g., as in Table II for $J = 7$) are also plotted in Fig. 5. The largest temporal pulse width in the present range of experimental conditions had an actual duration of $\tau_1/T = 0.5$, yielding a stroke ratio of $L_1/D = 4.09$ and ring velocity ratio of $r_{\text{ring},1} = 2.80$ with $U_\infty = 1.22$ m/s for $J = 7$ (blue markers); this placed the pulse in the regime of a vortex ring with a trailing column. Then, since the $u'_{j,\text{rms}}$ was constant for every pulsing condition, as the temporal pulse width was systematically decreased, the stroke ratio was reduced while the ring velocity ratio increased for a fixed jet momentum flux ratio. For the smallest temporal pulse widths explored, corresponding to the narrowest of the slow pulses and all of the fast pulses for the jet at $J = 7$, the stroke ratios of $L/D = 2.86$–2.56 and ring velocity ratios of $r_{\text{ring}} = 5.13$–4.46 placed the pulses in the regime of a vortex ring without a trailing column. From inspection of Fig. 5, it appeared that an actual temporal

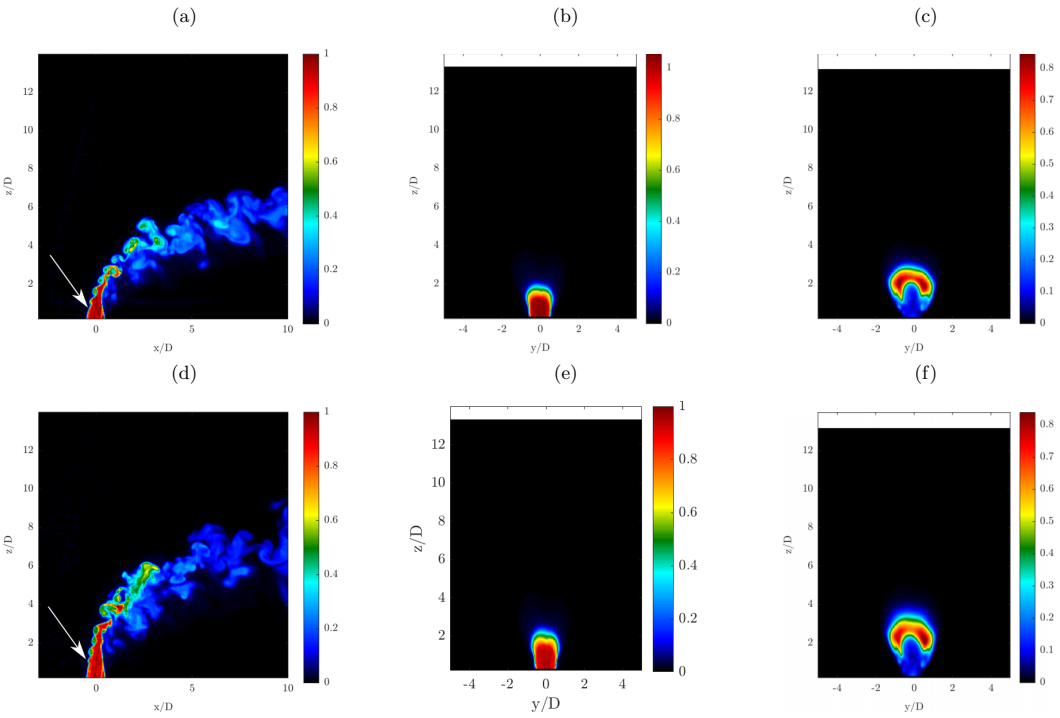

FIG. 6. Representative PLIF images of the unforced JICF at $J = 7$ [(a)–(c)] and at $J = 10$ [(d)–(f)], where (a) and (d) depict the instantaneous center-plane of the jet, and (b) and (e), and (c) and (f) are mean cross-sectional slices of the jet at $x/D = 0.0$ and 0.5, respectively. Included in (a) and (d) are white arrows denoting the approximate initial vortex rollup location in the USL.

pulse width of $\tau/T \approx 0.25$ at $J = 7$ would have produced a fully filled vortex ring, corresponding to a point on the "formation number" curve in Fig. 5, carrying the maximum amount of jet fluid possible without the generation of a trailing column. As the momentum flux ratio was increased to $J = 10$ (red markers) by reducing the magnitude of the cross-flow to $U_\infty = 1.05$ m/s, the stroke ratios remained unchanged compared with $J = 7$ conditions, while the ring velocity ratios were systematically increased by approximately 16%. With this change, each of the vortex rings formed in principle would have smaller trailing columns, or less fully filled vortex rings in the case of the $\tau/T = 0.20$ pulses, relative to those for the same temporal pulses for $J = 7$ conditions. This kind of change could be quite impactful since the amount of jet fluid carried by a ring or ring with a trailing column is known to significantly impact mixing, quantified by the rate of change in vortex ring total volume, for isolated vortex rings in cross-flow [44]. The present experiments explore the influence of the fullness of the vortex rings and the different effects of the double-pulse forcing when applied to the AU and CU transverse jets. In this section the structural alterations will be discussed, while the effects of mixing will be described in Sec. III C.

In the present experiments, three types of dynamical responses of the transverse jet to excitation were noted: vortex collisions, where the quick pulse clearly collided with the slow pulse; vortex interactions, where the quick pulse grazed or passed very close to the slow pulse; and no significant interaction, where the two pulses did not appear to interact or influence one another. Figure 6 shows representative instantaneous center-plane images of the unforced jet at $J = 7$ and 10, along with mean cross-sectional images for each case at downstream locations of $x/D = 0.0$ and 0.5. For these and subsequent PLIF images in this paper, the color-bar jet concentration maximum for the cross-sectional images was individually scaled to allow quantitative comparisons with the jet center-plane. In Fig. 6, both flow conditions the jets showed clear vortex rollup along the USL of the jet, with the

onset of the rollup appearing at $z/D = 0.5$ for $J = 7$ and $z/D = 0.7$ for $J = 10$, as approximately denoted via the arrows in Fig. 6, which was quantitatively consistent with the onset of the dominant USL instabilities measured by the hot-wire anemometer in Fig. 4. In the cross section, the jet in both cases had already begun to develop the characteristic CVP even by 0.5 diameters downstream, which for these relatively low-momentum flux ratios was quite symmetric. These representative depictions of the jet served as reference for the changes created by various forcing conditions.

Representative effects of excitation on jet structure are shown in Figs. 7–9, where instantaneous jet center-plane PLIF images have the same color bar as one another and mean cross-sectional PLIF images have color bars scaled for each image. Figure 7 shows a series of images for the jet evolution over a single forcing period for the double-pulse forcing case 1c, a case where the first (slow) pulse theoretically should correspond to a vortex with a trailing jet and the second (quick) pulse should correspond to a vortex without a trailing jet, per Fig. 5. For the images in Fig. 7, the instantaneous center-plane phase progression for the forcing period is shown at every tenth of a period. The first image [Fig. 7(a)] was approximately at the initiation of the slow pulse, $\theta = 0^\circ$; this and sequential images in Figs. 7(b)–7(f) show that the slow pulse generated a vortex ring with a trailing column, especially in Figs. 7(e)–7(f), and was tilted downstream. The quick pulse, seen in Figs. 7(g)–7(j), revealed the formation of a vortex ring without a distinct trailing column, with a slight upstream tilt. The qualitative characteristics of formation and tilting of the slow-pulse and quick-pulse vortex rings were consistent with the predicted behavior of isolated vortex rings in cross-flow and fully modulated JICFs for their corresponding vortex ring regimes in Fig. 5 [35,44]. And while the slow pulse was mainly formed and then convected downstream, the quick pulse penetrated more deeply into the flow field before being convected by the cross-flow. This was also consistent with the DNS for vortex rings in cross-flow, where Sau and Mahesh [44] suggest that a vortex ring with a stroke ratio L/D at or nearly at the formation number should produce the best penetration whereas larger stroke ratios, which produce vortex rings with trailing columns, do not penetrate as deeply. Interestingly, Sau and Mahesh [35] also suggest that, as the ring velocity ratio decreases and successive vortex rings are closer together, the forcing conditions producing the greatest overall penetration all collapse onto a single curve for stroke ratios below the ideal formation stroke ratio. Indeed, it can be seen in Figs. 7(g)–7(i) that as the quick pulse was formed, it propagated into the trailing column of the vortex ring for the slow pulse. As compared with quick pulses for other forcing conditions (to be shown), in which there were no significant interactions in the near field, the jet in Fig. 7 did not penetrate as deeply. In addition to colliding with the trailing column of the slow pulse, vortex rings also appeared to have a distinct collision in Figs. 7(h)–7(j), where the downstream portion of the quick vortex ring, having positive vorticity, collided with the upstream portion of the slow ring, which was of opposite sign. This effectively led to a breakdown of both vortex rings and, as such, this forcing case was classified as one with clear vortex collisions. In the mean cross-sectional images of the jet at $x/D = 0.0$ and 0.5 [Figs. 7(k)–7(l)] the jet clearly penetrated more deeply than the unforced jet [cf. Figs. 6(b) and 7(c)], despite the vortex collisions, where even at $x/D = 0.0$ the forced jet was already penetrating to almost $z/D = 8.0$. Interestingly, the jet still appeared to have some semblance of a CVP structure at $x/D = 0.5$, however, the concentration distribution was quite different from that of the unforced jet, where in Fig. 7(l) the resulting concentration appeared almost as two separate columns rather than one connected structure. The mean image thus appeared to represent the side lobes of the vortex rings as they were produced and propagated into the flow field; consistent with this, it was noted the concentration was found to dramatically decrease at about $z/D = 4.0$, where in the center-plane the two vortex rings collided.

PLIF images for an additional forcing case at $J = 7$ is depicted in Fig. 8, corresponding to conditions in which there were only slight interactions between the two vortex rings in a given period for the forcing case 2a waveform. As with the vortex collision case in Fig. 7, the series of figures commenced approximately at the initiation of the slow pulse $\theta = 0^\circ$, where subsequent snapshots were at every 36° over a single forcing period. The temporal pulse width of the slow pulse was approximately $\tau_1/T = 0.40$, theoretically corresponding to a vortex ring with a trailing

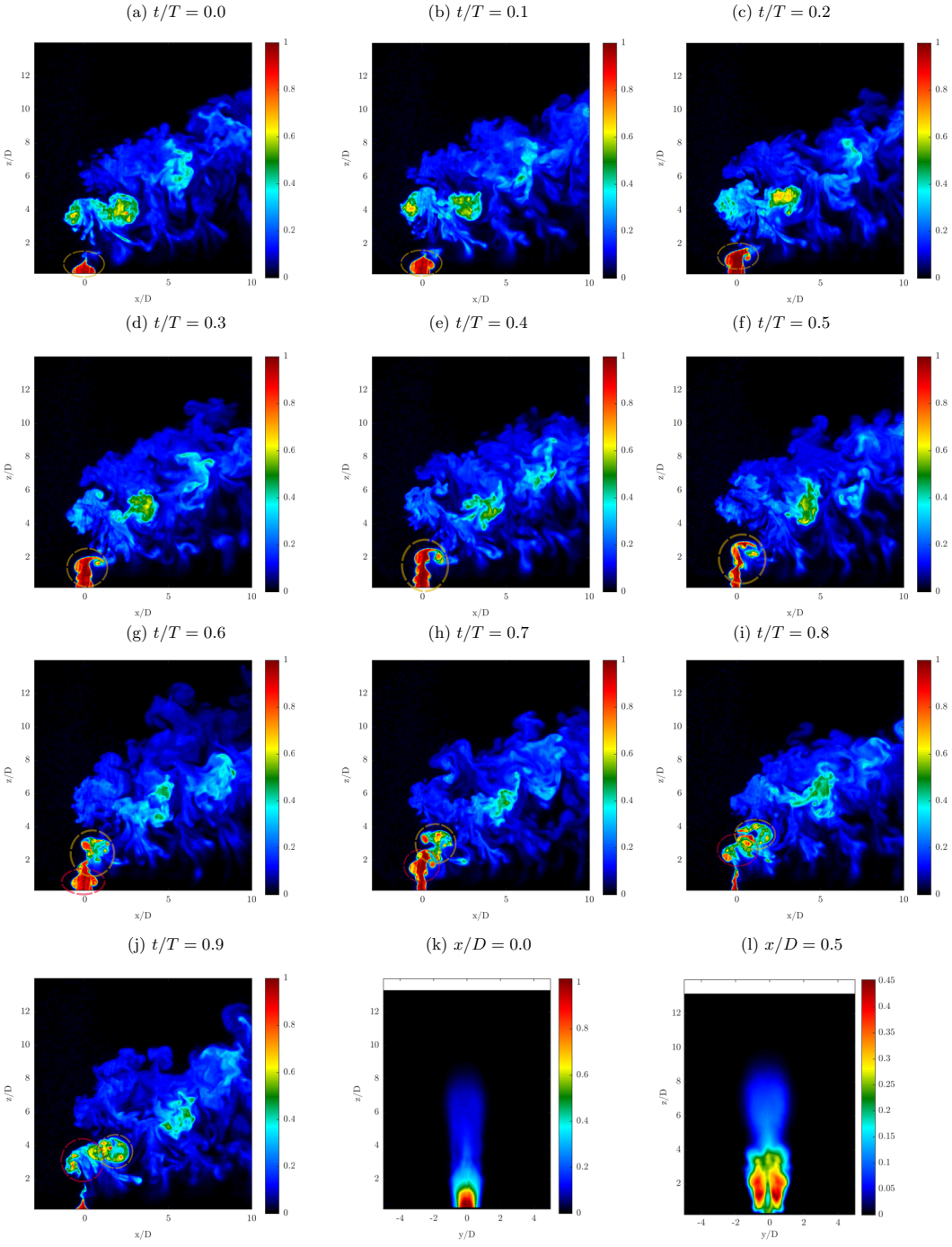

FIG. 7. Representative PLIF images of the double-pulse forced AU jet at $J = 7$, for forcing case 1c where (a)–(j) depict the instantaneous center-plane phase progression at every tenth of a the forcing period, and (k)–(l) are mean cross-sectional slices of the jet at $x/D = 0.0$ and 0.5, respectively. Yellow and red dashed circles represent slow and quick pulse structures, respectively.

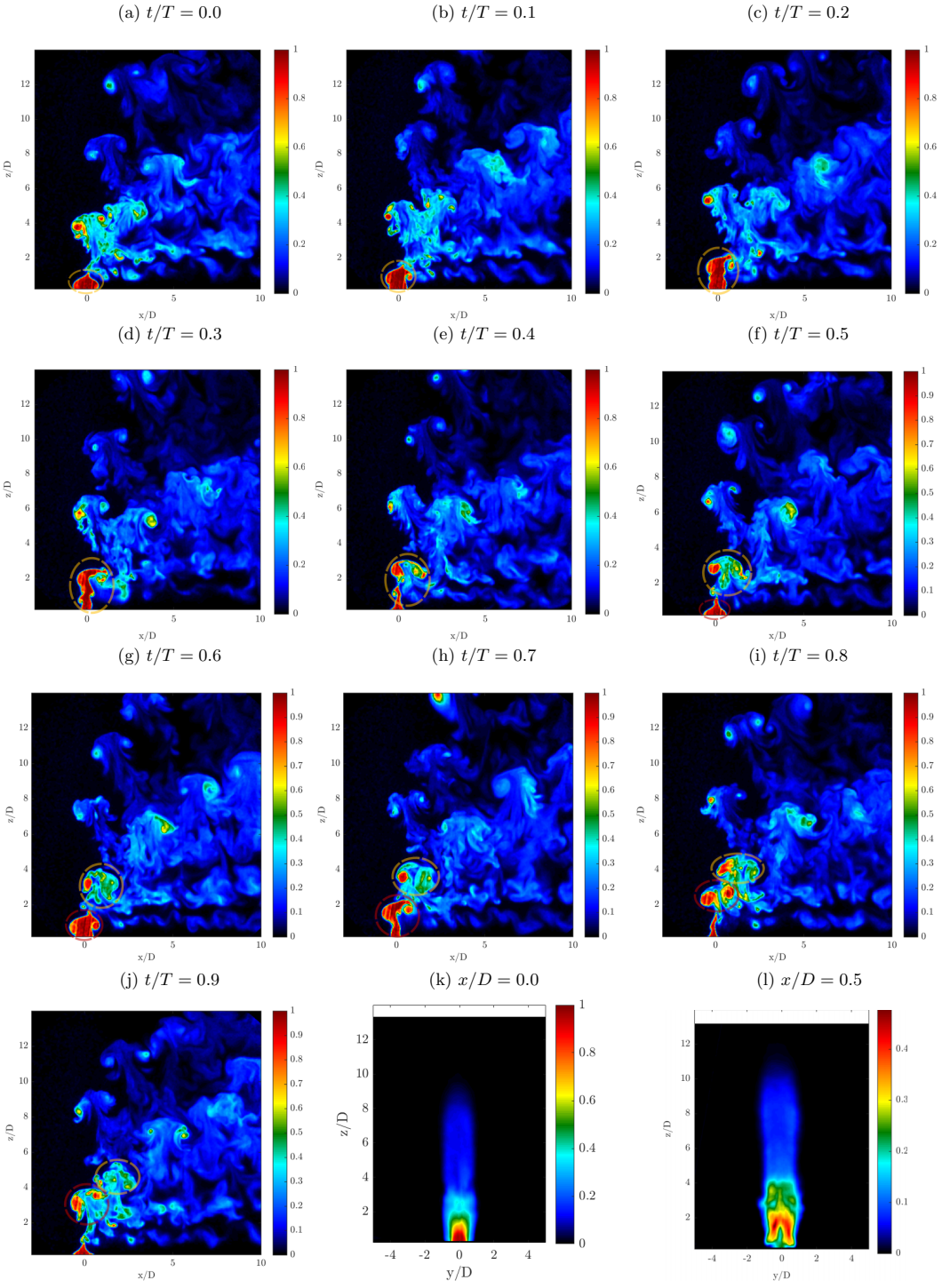

FIG. 8. Representative PLIF images of the double-pulse forced AU jet at $J = 7$, for forcing case 2a where (a)–(j) depict the instantaneous center-plane phase progression at every tenth of a the forcing period, and (k) and (l) are mean cross-sectional slices of the jet at $x/D = 0.0$ and 0.5, respectively. Yellow and red dashed circles represent slow and quick pulse structures, respectively.

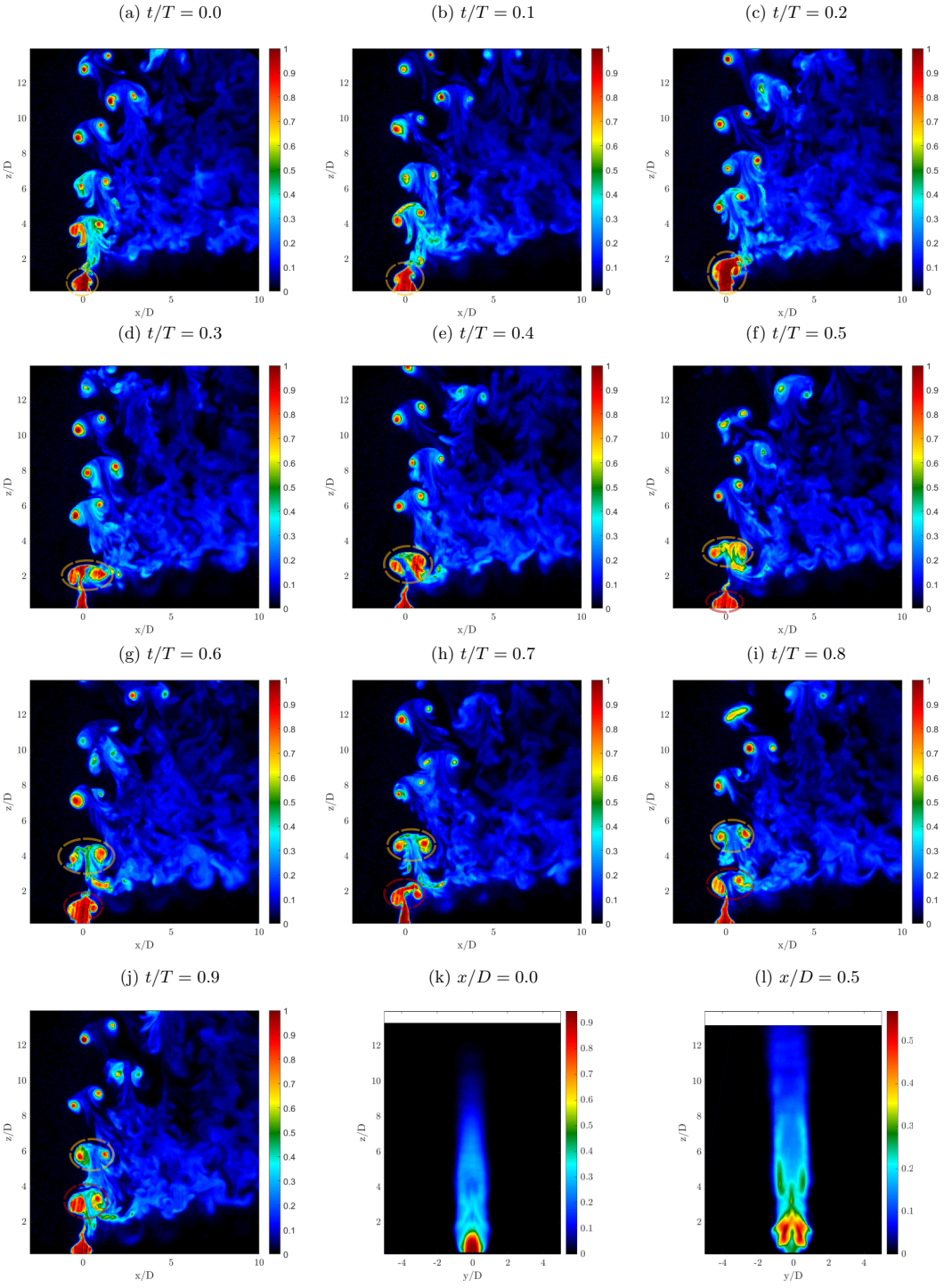

FIG. 9. Representative PLIF images of the double-pulse forced CU jet at $J = 10$, for forcing case 4a where (a)–(j) depict the instantaneous center-plane phase progression at every tenth of a the forcing period, and (k) and (l) are mean cross-sectional slices of the jet at $x/D = 0.0$ and 0.5, respectively. Yellow and red dashed circles represent slow- and quick-pulse structures, respectively.

column (per Fig. 5), and this was confirmed in Figs. 8(d)–8(f). As with the slow pulse considered in the case of vortex collisions, the resulting vortex ring was tilted downstream, and did not penetrate very deeply into the flow field. But, unlike the case of the vortex collisions in Fig. 7, when the quick pulse was formed, instead of colliding with upstream lobe of the main vortex ring, it cut directly through the trailing column and simply passed adjacent to the slow vortex ring [Figs. 8(g)–8(j) and 8(a)–8(c)], with only slight interaction. In interacting with the trailing column of the slow vortex ring, the downstream portions of the quick vortex ring were significantly weakened, seen in the scalar concentration in both the upstream and downstream portions of the vortex ring in Fig. 8(b). Due to the overall weakened interaction between the two vortex rings as compared with the case with vortex collisions, both rings were seen to have longer lifetimes and persisted further into the downstream, where in Fig. 8(j) the slow ring from the previous forcing period was present at the location $x/D \approx 5$ and $z/D \approx 7$, and the corresponding quick ring was at $x/D \approx 1$ and $z/D \approx 9$, though the quick ring completely propagated out of the FOV after enough time. In the cross section [Figs. 8(k) and 8(l)], the mean jet structure was generally similar to the case in Figs. 7(k) and 7(l), though unlike the vortex collisions case, the jet structure at $x/D = 0.5$ had a high concentration core region that had taken on more of the CVP-like shape, with a lesser vertical extent, though its overall mean jet structure was penetrated almost two jet diameters deeper into the flow field than seen in Fig. 7(l). These features were generally consistent with those observed computationally by Sau and Mahesh [35], who see distinct differences in the vortex ring stretching for ring-ring interactions compared with ring-trailing column interactions.

The last set of sample PLIF images for double-pulse forcing corresponds to conditions producing no significant interactions between successive vortex rings. Since this and other cases (Figs. 7 and 8) produced images that were similar between the different momentum flux ratios explored, for this condition we show results for $J = 10$ in Fig. 9 for forcing case 4a. For this forcing condition, the temporal pulse widths of both the slow and quick pulses were matched at $\tau/T = 0.2$, where the resulting vortex rings, according to the regime map in Fig. 5, corresponded to vortex rings without a trailing column. In matching the temporal pulse width between the two pulses, the waveform was effectively square-wave forcing at 110 Hz with a duty cycle of $\alpha = 30\%$; however, the temporal spacing was such that they were not evenly distributed over a single forcing period, again with the aim of affecting vortex interaction. The resulting quick- and slow-pulse formations are seen in Figs. 9(i), 9(j) and 9(a)–9(c) and 9(d)–9(g), respectively, where in both cases the rings formed without a distinct trailing column and were slightly tilted upstream. Given the lack of a trailing column, and spacing between the pulses, the vortex rings did not interact, and as a result propagated quite deeply and independently into the flow field; this is similarly observed for case 4a with $J = 7$. With a relatively long "off" duration of $\Delta\tau_{2\to1}/T = 0.45$ of the forcing period, the vortex rings penetrated quite distinctly, yet because the jet was not quite fully modulated, the small amount of jet fluid exiting the nozzle between pulses appeared to stay relatively close to the floor of the test section, more so in the case with $J = 7$. Consistent with earlier JICF experiments with axisymmetric square-wave forcing [38], as well as simulations [35], the jet fluid which issues when the forcing waveform is not actively being pulsed lacks momentum, especially when contrasted with the high-momentum carrying vortex rings, resulting in a highly bifurcated jet. For the mean cross-sectional images of the jet [Figs. 9(k) and 9(l)], the jet structure in the core region at $z/D = 0.5$ was similar in shape to that of the pulsation case producing minimal interactions [e.g., as in Fig. 8(l)]; the same was observed for the case with $J = 7$. A significant mean penetration of the jet in the near field was observed in Figs. 9(k) and 9(l), as expected, especially for this larger value of J than in Figs. 7 and 8.

Table III lists the various types of vortex ring collisions, interactions, or lack thereof which were visually distinguished for the different double-pulse forcing conditions explored experimentally, for both the AU and CU unforced jets at $J = 7$ and 10, respectively. Interestingly, as the momentum flux ratio was decreased from $J = 10$ to 7, corresponding to an increase in the cross-flow velocity U_∞, the vortex interactions for a given waveform appeared to be strengthened, in some cases transitioning from interactions between the rings or the ring and trailing column to actual collisions of the rings. This transition in the degree of interaction between the rings was consistent with a

TABLE III. Observed behavior of vortices generated by the transverse jet in response to various double-pulse forcing waveforms corresponding to case labels described in Tables I and II.

Forcing case	$J = 7$	$J = 10$
1a	Collision	Interaction
1b	Collision	Interaction/collision
1c	Collision (Fig. 7)	Collision
2a	Interaction (Fig. 8)	Interaction
2b	Interaction	Interaction
2c	Interaction	Interaction
3a	Interaction/collision	Interaction/collision
3b	Collision	Interaction/collision
3c	Collision	Interaction/collision
4a	No interaction	No interaction (Fig. 9)
4b	Interaction/collision	Interaction
4c	Collision	Collision

reduction in the ring velocity ratio, recalling from Fig. 5 that going from $J = 10$ (red symbols) to $J = 7$ (blue symbols) corresponded to a change in r_{ring} of approximately 16%, which in turn resulted in the vortex rings being more fully filled or developing larger trailing columns, depending on the originating vortex ring regime for a given pulse width. Adding to the jet trailing column is thought to produce a slower-moving vortex ring which does not penetrate as deeply, while an underfilled vortex ring which is made fuller, approaching a fully filled isolated vortex ring, will actually propagate faster and penetrate deeper [35]. One could then conjecture that in decreasing the momentum flux ratio, the slow vortex rings were made slower (with the exception of the $\tau_1/T = 0.20$ cases), which did not have trailing columns, and the fast pulses were made faster, thereby enhancing the vortex ring interactions and/or collisions as summarized in Table III. Hence, many of the trends observed in the dynamics of vortical structures formed in the present transverse jet experiments were consistent with those predicted computationally for vortex rings in cross-flow [35,44].

C. Mixing quantification

The effective mixing between the jet and cross-flow was determined using both the molecular mixing quantification based on the instantaneous unmixedness parameter (U), as well as the overall jet penetration. Both could be determined quantitatively via the scalar PLIF imaging in the jet center-plane. Calculating the unmixedness, which as noted earlier represents the second moment of the scalar concentration field, was performed with Eq. (4), such that lower unmixedness corresponds to better molecular mixing. Local mean jet vertical penetration z_p/D was based on the bounding region of the jet as defined by a 3% threshold of the jet concentration normalized by the concentration at the jet core. For each of these evaluations of the flow, the validity became less reliable after approximately $x/D = 5.0$ because certain jet forcing cases were found to propagate out of the FOV (at a height of $z/D \approx 14.0$) captured in the PLIF images. Yet, because of the present emphasis on the influence of vortex interactions on jet dynamics and mixing, the current data trends were still found to provide useful comparisons.

Figures 10 and 11 present results for mixing metrics associated with the $J = 7$ and 10 cases, respectively. For jet penetration, in Fig. 10(a), which shows the variation in penetration height z_p/D with downstream distance for $J = 7$, forcing cases in which the interactions between the vortex rings were minimal, or did not exist (e.g., as in case 4b), resulted in the greatest penetration of the jet. Likewise, cases with strong vortex collisions (e.g., as in case 1c) generally resulted in a lower overall penetration of the jet. Enlarging the temporal spacing between the slow and quick pulses for all slow-pulse temporal pulse widths, with one notable exception, acted to systematically

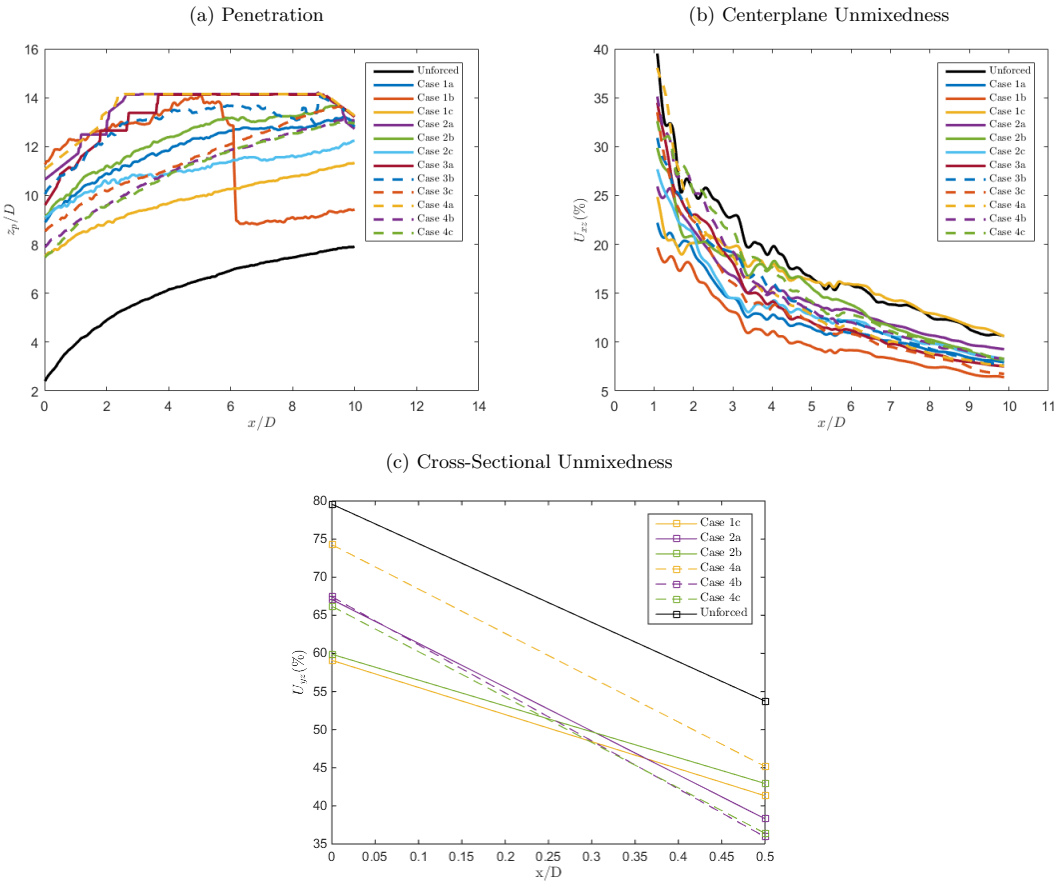

FIG. 10. Mixing metrics for various excitation cases at $J = 7$: (a) mean center-line vertical jet penetration z_p/D; and downstream evolution of unmixedness U evaluated in (b) the center-plane and (c) the jet cross-section, with averaging over 600 instantaneous images.

increase the penetration of the jet, quantitatively in agreement with the structural trends discussed earlier. The lone exception was for the slow temporal pulse width of approximately $\tau_1/T = 0.50$, in case 1c, where increasing the temporal spacing between the slow and quick pulses reduced the subsequent spacing between the quick pulse and the slow pulse in the following temporal forcing period. This effectively resulted in inducing vortex interactions for case 1c, and thus did not enhance the penetration as much as the more balanced temporal spacing in cases 1a or 1b. The notable drop in penetration for this latter case at $x/D \approx 6.0$ resulted from the concentration intensity in the quick pulse dropping below the 3% threshold as a result of the mixing and entrainment processes of the ring. Hence, this unusual trend was related to the threshold selection rather than the actual vortex dynamics. In results for jet penetration for $J = 10$ in Fig. 11(a), one sees very similar trends to those in Fig. 10(a), in that as the temporal pulse width of the slow pulse was decreased and the temporal spacing between pulses enlarged, thus reducing the near-field vortex interactions, the jet penetration was significantly enhanced over that of the unforced jet and other forcing cases. Separate quantification of jet spread by Harris [49] followed generally similar trends to those of the overall penetration.

Molecular mixing trends for the naturally AU $J = 7$ jet, shown using the center-plane unmixedness parameter U_{xz} in Fig. 10(b), and the cross-sectional unmixedness U_{yz} in Fig. 10(c), suggested

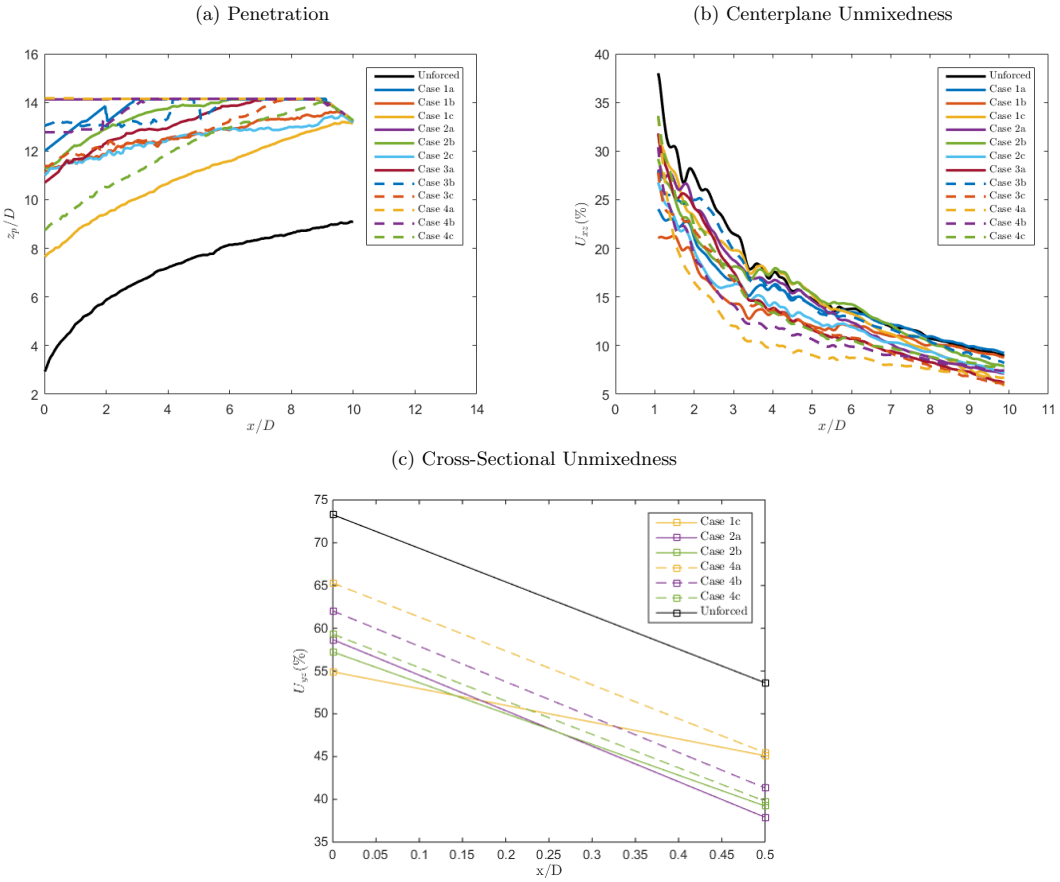

FIG. 11. Mixing metrics for various excitation cases at $J = 10$: (a) mean center-line vertical jet penetration z_p/D; and downstream evolution of unmixedness U evaluated in (b) the center-plane and (c) the jet cross-section, with averaging over 600 instantaneous images.

that all forcing cases enhanced the overall mixing as compared with the unforced jet, since in virtually all forcing cases the unmixedness was lower than that without forcing. While U_{yz} was only extracted from two locations, at the center of the jet exit ($x/D = 0.0$) and at the downstream edge of the jet exit ($x/D = 0.5$), the significant mixing improvement with excitation, and magnitudes of unmixedness, were consistent with center-plane image-based results beginning at one diameter downstream of injection. The greatest effect of excitation for the AU case in Fig. 10 was observed in the near field, within 3 diameters of injection, as seen in other forced JICF experiments [37,38,53]. For the present experiment, however, both the structure of the individual vortical structures and the type of interaction of vortices, which could not be studied in earlier experiments, were found to influence molecular mixing. The best molecular mixing (lowest U) for $J = 7$ was observed for the 1b forcing case, which had the largest slow-pulse temporal pulse width investigated, with an actual $\tau_1/T \approx 0.50$, producing a dominant jet trailing column. Good molecular mixing was also seen in case 1a, with the same vortex structure and a slightly longer spacing between slow and quick pulses as for 1b. As the temporal pulse width of the slow pulse was systematically decreased, as one changes from case 1 to 2 and eventually to case 4, the enhancement in center-plane mixing in particular was decreased, where worse mixing was seen for the forcing cases labeled 4, where both pulses were approximately at $\tau/T = 0.2$, corresponding to vortex rings without trailing columns. This observation agreed with simulations Sau and Mahesh [44], whose studies

indicate that single vortex rings in cross-flow with trailing columns actually mix more vigorously than a fully filled or underfilled vortex ring due to entrainment into the column. Interestingly, in examining all of the forcing cases with a slow temporal pulse width near $\tau_1/T \approx 0.50$ (cases labeled 1), one finds dramatically different enhancements to the molecular mixing. As the temporal spacing between the slow and quick pulses was reduced, the magnitude of center-plane unmixedness increased, for example, where the 1c case was actually among the worst mixed, and even eventually developed about the same degree of mixing as the unforced jet further downstream. For $J = 7$ in Fig. 10(b), the overall best molecular mixing tended to occur for the most active vortex collisions or interactions, especially for vortices with trailing columns, yet it is important to note that pulse width as well as pulse spacing contribute to these effects. It is also important to note that forcing conditions which resulted in the best molecular mixing did not usually correspond to conditions of maximum jet penetration, as observed in other forced as well as passively controlled transverse jet experiments [37,38,50]. Importantly, this observation contradicts long held assumptions that improvements in jet penetration correspond to improved molecular mixing [1].

Finally, Figs. 11(b) and 11(c) show the effects of double-pulse forcing conditions on molecular mixing in two planes for the naturally CU jet at $J = 10$. Here, the enhancement in mixing over the unforced jet also took place with such excitation, as observed for the $J = 7$ jet [Figs. 10(b) and 10(c)], and the unmixedness convergence downstream was even more prominent at $J = 10$. The best molecular mixers for $J = 10$ for the majority of the flow field in Fig. 11(c) appeared to be the 4a and 4b forcing cases, with minimal vortex interactions, though both of these conditions had jet fluid which penetrated out of the FOV very early on in the jet evolution, and thus may not be as reliable mixing quantifications as for other cases. Remarkably, even discounting these cases, the forcing conditions which resulted in the best molecular mixing of the jet were not always the same as those which optimized mixing for the $J = 7$ jet. Aside from cases 4a and 4b, Fig. 11(b) indicates that excitation with a longer slow pulse, case 1b, did produce significant improvements in molecular mixing, as was the case for $J = 7$, and once again, case 1c, which did involve vortex collisions, was less well mixed and did not constitute a significant improvement in mixing over the unforced JICF. In addition, however, forcing cases with a slow-pulse temporal pulse width of around $\tau_1/T = 0.30$, such as case 3a, associated with a vortex ring with a very small trailing column, produced very good molecular mixing. From the jet structural characteristics in Table III, these conditions corresponded to cases where there were relatively strong interactions between the slow and quick vortex rings. While the forcing cases for optimal molecular mixing were not precisely the same for $J = 10$ as for $J = 7$, one would not expect this to always be consistent, given the natural instabilities for each being different (CU vs AU, respectively). But, the results here underscore the importance of controlling the vortex ring interactions, both through pulse width and temporal separation, to control jet mixing. Overall, however, for both momentum flux ratios, conditions where there were typically greater vortex interactions and collisions appeared to create improved molecular mixing in the transverse jet.

IV. DISCUSSION AND CONCLUSIONS

This experimental study documented the effects of controlled vortex interactions associated with a jet in cross-flow via a double-pulse forcing waveform, wherein two distinct temporal pulses were generated during a single forcing period. Effects of controlled vortex generation and interactions on jet structure and mixing were quantified for both a transitionally convectively and absolutely unstable jet ($J = 10$), and a jet which was clearly absolutely unstable ($J = 7$). Depending on relative pulse widths and temporal separation of pulses, the application of such excitation was seen to dramatically improve jet penetration as well as molecular mixing, though not always under the same conditions.

As noted in the results of this study, conditions for which transverse jet behavior could achieve enhanced penetration (important in many applications) and/or improved molecular mixing (important in some but not all of the same applications) depended on the nature of the vortex rings that

were formed and the ability of such rings to interact, fully collide, or avoid one another in sequence. Many of the results are consistent with the effects of the degree of filling of a vortex ring and the presence of a trailing column of jet fluid as explored in the DNS studies of Sau and Mahesh [44] for a single vortex in cross-flow. Yet, for the transverse jet, with the present approach's ability to alter both vortex fill and sequential vortex interactions, an additional level of flow control was introduced. While acetone PLIF as a diagnostic enabled the ability to study jet structure as well as molecular mixing to a fair degree of accuracy, the nature of the detailed vorticity as well as jet shear layer and structural dynamics, and their relationship to optimized behavior, is also important. This is the subject of ongoing studies, through which a more complete picture of optimized vortex generation in transverse jets may be developed.

ACKNOWLEDGMENT

This research has been supported by the National Science Foundation under Grants No. CBET-1437014 and No. CBET-1933310 and by the Air Force Office of Scientific Research under Grants No. FA9550-15-1-0261 and No. FA9550-19-1-0191.

The authors report no conflict of interest.

[1] R. J. Margason, Fifty years of jet in cross-flow research, AGARD-CP-534 (1993).
[2] A. R. Karagozian, Transverse jets and their control, Prog. Energy Combust. Sci. **36**, 531 (2010).
[3] K. Mahesh, The interaction of jets with crossflow, Annu. Rev. Fluid Mech. **45**, 379 (2013).
[4] A. R. Karagozian, The jet in crossflow, Phys. Fluids **26**, 101303 (2014).
[5] T. A. Brzustowski, S. Gollahalli, and H. Sullivan, The turbulent hydrogen diffusion flame in a crosswind, Combust. Sci. Technol. **11**, 29 (1975).
[6] A. R. Karagozian, An analytical model for the vorticity associated with a transverse jet, AIAA J. **24**, 429 (1986).
[7] J. D. Holdeman, Mixing of multiple jets in a confined subsonic crossflow, Prog. Energy Combust. Sci. **19**, 31 (1993).
[8] J. P. Bons, R. Sondergaard, and R. B. River, The fluid dynamics of lpt blade separation control using pulsed jets, J. Turbomachinery **124**, 77 (2002).
[9] S. V. Ekkad, S. Ou, and R. B. River, Effect of jet pulsation and duty cycle on film cooling from a single jet on a leading edge model, J. Turbomachinery **128**, 564 (2006).
[10] T. S. Oh and J. A. Schetz, Finite element simulation of complex jets in a crossflow for v/stol applications, J. Aircraft **27**, 389 (1990).
[11] D. N. Miller, P. J. Yagle, and J. W. Hamstra, Fluidic throat skewing for thrust vectoring in fixed-geometry nozzles, AIAA Conference paper 99-0365, January (1999).
[12] J. M. M. Barata, Multiple jet/wall/cross-wind interaction relevant to vstol ground effects, *AIAA Aviation Forum* (AIAA, Reston, VA, 2013).
[13] T. F. Fric and A. Roshko, Vortical structure in the wake of a transverse jet, J. Fluid Mech. **279**, 1 (1994).
[14] Y. Kamotani and I. Greber, Experiments on a turbulent jet in a cross flow, AIAA J. **10**, 1425 (1972).
[15] S. Megerian, J. Davitian, L. de B. Alves, and A. R. Karagozian, Transverse-jet shear-layer instabilities. part 1. experimental studies, J. Fluid Mech. **593**, 93 (2007).
[16] J. Davitian, D. Getsinger, C. Hendrickson, and A. R. Karagozian, Transition to global instability in transverse-jet shear layers, J. Fluid Mech. **661**, 294 (2010a).
[17] D. R. Getsinger, C. Hendrickson, and A. R. Karagozian, Shear layer instabilities in -density transverse jets, Exp. Fluids **53**, 783 (2012).
[18] T. Shoji, E. W. Harris, A. Besnard, S. G. Schein, and A. R. Karagozian, On the origins of transverse shear layer instability transition, J. Fluid Mech. **890** (2020).
[19] L. Cortelezzi and A. R. Karagozian, On the formation of the counter-rotating vortex pair in transverse jets, J. Fluid Mech. **446**, 347 (2001).

[20] S. Bagheri, P. Schlatter, P. J. Schmid, and D. S. Henningson, Global stability of a jet in crossflow, J. Fluid Mech. **624**, 33 (2009).
[21] P. Schlatter, S. Bagheri, and D. S. Henningson, Self-sustained global oscillations in a jet in crossflow, Theor. Comput. Fluid Dyn. **25**, 129 (2011).
[22] P. S. Iyer and K. Mahesh, A numerical study of shear layer characteristics for low-speed transverse jets, J. Fluid Mech. **790**, 275 (2016).
[23] M. A. Regan and K. Mahesh, Global linear stability analysis of jets in cross-flow, J. Fluid Mech. **828**, 812 (2017).
[24] L. S. d. B. Alves, R. E. Kelly, and A. R. Karagozian, Local stability analysis of an inviscid transverse jet, J. Fluid Mech. **581**, 401 (2007).
[25] M. Ilak, P. Schlatter, S. Bagheri, and D. S. Henningson, Bifurcation and stability analysis of a jet in crossflow, J. Fluid Mech. **696**, 94 (2012).
[26] D. B. d. Souza, R. B. Freitas, and L. S. d. B. Alves, A criterion for the linear convective to absolute instability transition of a jet in crossflow: the countercurrent viscous and round mixing layer analogy, Phys. Rev. Fluids **6**, L041901(2021).
[27] R. M. Kelso, T. T. Lim, and A. E. Perry, An experimental study of round jets in cross-flow, J. Fluid Mech. **306**, 111 (1996).
[28] Y. M. Marzouk and A. F. Ghoniem, Vorticity structure and evolution in a transverse jet, J. Fluid Mech. **575**, 267 (2007).
[29] D. R. Getsinger, L. Gevorkyan, O. Smith, and A. R. Karagozian, Structural and stability characteristics of jets in crossflow, J. Fluid Mech. **760**, 342 (2014).
[30] L. Gevorkyan, T. Shoji, D. R. Getsinger, O. I. Smith, and A. R. Karagozian, Transverse jet mixing characteristics, J. Fluid Mech. **790**, 237 (2016).
[31] H. Johari, M. Pacheco-Tougas, and J. C. Hermanson, Penetration and mixing of fully modulated turbulent jets in crossflow, AIAA J. **37**, 842 (1999).
[32] R. T. M'Closkey, J. King, L. Cortelezzi, and A. R. Karagozian, The actively controlled jet in crossflow, J. Fluid Mech. **452**, 325 (2002).
[33] S. Shapiro, J. King, R. T. M'Closkey, and A. R. Karagozian, Optimization of controlled jets in crossflow, AIAA J. **44**, 1292 (2006).
[34] F. Muldoon and S. Acharya, Direct numerical simulation of pulsed jets in crossflow, Comput. Fluids **39**, 1745 (2010).
[35] R. Sau and K. Mahesh, Optimization of pulsed jets in crossflow, J. Fluid Mech. **653**, 365 (2010).
[36] J. Davitian, C. Hendrickson, D. Getsinger, R. T. M'Closkey, and A. R. Karagozian, Strategic control of transverse jet shear layer instabilities, AIAA J. **48**, 2145 (2010b).
[37] T. Shoji, E. W. Harris, A. Besnard, and A. R. Karagozian, Effects of sinusoidal excitation on transverse jet dynamics, structure and mixing, AIAA J. **58**, 3889 (2020).
[38] T. Shoji, A. Besnard, E. W. Harris, R. T. M'Closkey, and A. R. Karagozian, Effects of axisymetric square-wave excitation on transverse jet structure and mixing, AIAA J. **57**, 1862 (2019).
[39] T. Shoji, E. W. Harris, A. Besnard, S. G. Schein, and A. R. Karagozian, Transverse jet lock-in and quasiperiodicity, Phys. Rev. Fuids **5**, 013901 (2020).
[40] L. K. B. Li and M. P. Juniper, Lock-in and quasiperiodicity in a forced hydrodynamically self-excited jet, J. Fluid Mech. **726**, 624 (2013a).
[41] X. Yang and A. Zebib, Absolute and convective instability of a cylinder wake, Phys. Fluids **1**, 689 (1989).
[42] M. Gharib, E. Rambod, and K. Shariff, A universal time scale for vortex ring formation, J. Fluid Mech. **360**, 121 (1998).
[43] H. Johari, Scaling of fully pulsed jets in crossflow, AIAA J. **44**, 2719 (2006).
[44] R. Sau and K. Mahesh, Dynamics and mixing of vortex rings in crossflow, J. Fluid Mech. **604**, 389 (2008).
[45] L. Gevorkyan, Structure and Mixing Characterization of Variable Density Transverse Jet Flows, Ph.D. thesis, University of California, Los Angeles, 2015.
[46] L. Gevorkyan, T. Shoji, W. Y. Peng, and A. R. Karagozian, Influence of the velocity field on scalar transport in gaseous transverse jets, J. Fluid Mech. **834**, 173 (2018).

[47] C. Hendrickson, Identification and Control of the Jet in Crossflow, Ph.D. thesis, University of California, Los Angeles, 2012.
[48] T. Shoji, Mixing and Structural Characteristics of Unforced and Forced Jets in Crossflow, Ph.D. thesis, University of California, Los Angeles, 2017.
[49] E. W. Harris, Structure, Mixing, and Dynamics of Controlled Single and Coaxial Jets in Crossflow, Ph.D. thesis, University of California, Los Angeles, 2020.
[50] E. W. Harris, A. Besnard, and A. R. Karagozian, Effect of tabs on transverse jet instabilities, structure, vorticity dynamics and mixing, J. Fluid Mech. **918**, A8 (2021).
[51] S. H. Smith and M. G. Mungal, Mixing, structure, and scaling of the jet in crossflow, J. Fluid Mech. **357**, 83 (1998).
[52] J. Shan and P. Dimotakis, Reynolds-number effects and anisotropy in transverse-jet mixing, J. Fluid Mech. **566**, 47 (2006).
[53] A. Besnard, External Asymmetric Forcing of Convectively Unstable Transverse Jets, Ph.D. thesis, University of California, Los Angeles (2019).
[54] P. E. Dimotakis and P. L. Miller, Some consequences of the boundedness of scalar fluctuations, Phys. Fluids **2**, 1919 (1990).
[55] A. K. M. F. Hussain and K. M. Q. Zaman, The free shear layer tone phenomenon and probe interference, J. Fluid Mech. **87**, 349 (1978).